JACS
JOURNAL OF THE AMERICAN CHEMICAL SOCIETY
Article
pubs.acs.org/JACS

Long-Range Electron Transfer Triggers Mechanistic Differences between Iron(IV)-Oxo and Iron(IV)-Imido Oxidants

Suresh Kumar,[†] Abayomi S. Faponle,[‡] Prasenjit Barman,[⊥] Anil Kumar Vardhaman,[⊥] Chivukula V. Sastri,*[,⊥] Devesh Kumar,*[,†] and Sam P. de Visser*[,‡]

[†]Department of Applied Physics, School for Physical Sciences, Babasaheb Bhimrao Ambedkar University, Vidya Vihar, Rae Bareilly Road, Lucknow, 226025 Uttar Pradesh, India

[⊥]Department of Chemistry, Indian Institute of Technology Guwahati, Assam 781039, India

[‡]Manchester Institute of Biotechnology and School of Chemical Engineering and Analytical Science, The University of Manchester, 131 Princess Street, Manchester M1 7DN, United Kingdom

Supporting Information

ABSTRACT: Nature often utilizes molecular oxygen for oxidation reactions through monoxygenases and dioxygenases. In many of these systems, a high-valent iron(IV)-oxo active species is found. In recent years, evidence has accumulated of possible iron(IV)-imido and iron(V)-nitrido intermediates in enzymatic catalysis, although little is known about their activity. In this work, we report a detailed combined kinetics and computational study on the difference in reactivity and chemical properties of nonheme iron(IV)-oxo compared with iron(IV)-tosylimido. We show here that iron(IV)-tosylimido complex is much more reactive with sulfides than the corresponding iron(IV)-oxo complex; however, the reverse trend is obtained for hydrogen atom abstraction reactions. The latter proceed with a relatively small kinetic isotope effect of k_H/k_D = 7 for the iron(IV)-tosylimido complex. Moreover, a Hammett analysis of hydrogen atom abstraction from para-X-benzyl alcohol reveals a slope of close to zero for the iron(IV)-oxo, whereas a strong negative slope is found for the iron(IV)-tosylimido complex. These studies implicate dramatic changes in the reaction mechanisms and suggest a considerable charge transfer in the transition states. Density functional theory calculations were performed to support the experiments and confirm an initial long-range electron transfer for the iron(IV)-tosylimido complex with substrates, due to a substantially larger electron affinity compared with the iron(IV)-oxo species. As a consequence, it also reacts more efficiently in electrophilic addition reactions such as those with sulfides. By contrast, the long-range electron transfer for the iron(IV)-tosylimido complex results in a rate constant that is dependent on the $\pi^*_{xz} \rightarrow \sigma^*_{z^2}$ excitation energy, which raises the hydrogen atom abstraction barrier above that found for the iron(IV)-oxo. On the other hand, sulfimidation has much earlier electron transfer steps with respect to sulfoxidation. All data has been analyzed and rationalized with valence bond models and thermochemical cycles. Our studies highlight the catalytic potential of iron(IV)-tosylimido complexes in chemistry and biology.

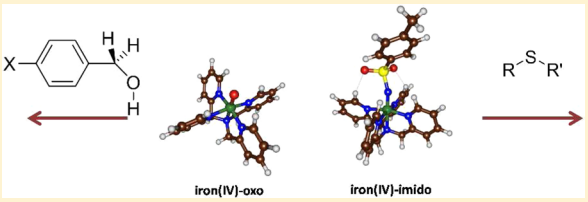

INTRODUCTION

Monoxygenases and dioxygenases are common enzymes in biology that utilize molecular oxygen usually on a transition metal center that can be bound into either a heme or nonheme environment.[1,2] A well-studied class of monoxygenases are the cytochromes P450 (P450s) that are found in all forms of life and catalyze the regioselective and stereospecific hydroxylation and epoxidation of substrates. These reactions have important functions in biology that include the biosynthesis of hormones in the liver, as well as the detoxification of metabolites and xenobiotics, such as drug molecules, in the body.[3] As such there is interest in understanding their function and mechanism from a pharmaceutical as well as biotechnological viewpoint. The P450s form a high-valent iron(IV)-oxo heme cation radical species in the catalytic cycle that is called compound I (Cpd I),[4] which is a highly reactive oxidant that reacts with substrates through aliphatic and aromatic hydroxylation, N-dealkylation, and sulfoxidation reactions.[5]

Despite the fact that much research has been devoted to P450 catalysis and synthetic model complexes there are still major gaps in our understanding of its catalytic mechanism and function. For instance, why does nature use molecular oxygen in the catalytic cycle of P450 enzymes and not, for instance, nitrogen, which is more abundant in the atmosphere? Technically, an iron(IV)-imido (Fe^{IV}═NR, R = alkyl) or iron(V)-nitrido (Fe^{V}≡N) complex should be a stable intermediate in P450 catalyzed reactions. Moreover, an iron(IV)-imido or iron(V)-nitrido could be reactive in NR group reactivity to substrates analogous to Cpd I. Indeed, over the years several examples in P450 catalysis, for example, in

Received: August 16, 2014
Published: November 12, 2014

dx.doi.org/10.1021/ja508403w | J. Am. Chem. Soc. 2014, 136, 17102−17115

aziridation and imidation reactions, have been reported that include an iron(IV)-nitrido intermediate.[6] For example, the reaction of iron(III)-porphyrin complexes with *N*-tosyliminophenyliodinane (PhINTs) in the presence of olefins led to efficient aziridination of the substrate. More recent work on the amination of substrates by engineered $P450_{BM3}$ enzymes gave several examples of efficient nitrogen group transfer reactions.[7]

Despite being relatively rare in enzymology, actually in inorganic chemistry there are many examples of high-valent metal-imido and metal-nitrido complexes, where they have been shown to be reactive in various processes.[8] Bioinspired P450 analogues have been developed to understand the chemical and physical properties of the active species of P450 enzymes.[9] In a number of these synthetic complexes an iron-nitrido or iron-imido complex could be formed, spectroscopically characterized, and studied for reactivity with selected substrates.[10] In addition, studies have been reported on high-valent ruthenium-nitrido porphyrin complexes, which were shown to efficiently activate sp^3 hybridized C−H bonds of substrates.[11]

In more recent work, attention has shifted to nonheme iron and ruthenium based nitrido and imido complexes. These structures range from pentacoordinated to heptacoordinated iron complexes and have been spectroscopically characterized.[12] The studies showed that aliphatic substrates with a C−H bond strength analogous to that of cyclohexane could be activated efficiently. In addition to mononuclear iron and ruthenium complexes, evidence of diiron(III,IV)-tosylimido complexes has also been reported.[13] Thus, Latour and coworkers[13] observed hydrogen atom abstraction and nitrene transfer reactions by the diiron(III,IV)-tosylimido complex efficiently, whereby the sulfimidation of *para*-substituted thioanisoles was found to correlate linearly with the Hammett constant in an electrophilic pathway.

The iron(IV)-tosylimido (NTs) complex, tosylimido = NTs, with pentadentate N4Py ligand (N4Py = *N*,*N*-bis(2-pyridylmethyl)-*N*-bis(2-pyridyl) methylamine) was synthesized by Klinker et al.[14] and spectroscopically characterized with UV−vis, NMR, EPR, EXAFS, and Mössbauer spectroscopies. Because the analogous iron(IV)-oxo species is also known, we used the opportunity to study the reactivity of $[Fe^{IV}(O)(N4Py)]^{2+}$ (**1**) versus $[Fe^{IV}(NTs)(N4Py)]^{2+}$ (**2**), Figure 1, against selected substrates.[15] It is found that the iron(IV)-oxo oxidant is more effective in hydrogen atom abstraction reactions, but the iron(IV)-tosylimido species, surprisingly, is seen to be much more reactive with sulfides. The intricate details of the catalysts that are responsible for these reactivity differences between **1** and **2** could not be established in detail in our previous study; therefore, we decided to follow up our original study with a broader substrate range, as well as a comprehensive computational study on the reactivity of **1** and **2** with either sulfides (dimethylsulfide, DMS) or hydrogen abstraction donors. We show here, for the first time, that iron(IV)-oxo and iron(IV)-tosylimido have different valence orbital shapes, which lead to differences in electron affinity values that trigger reactivity changes.

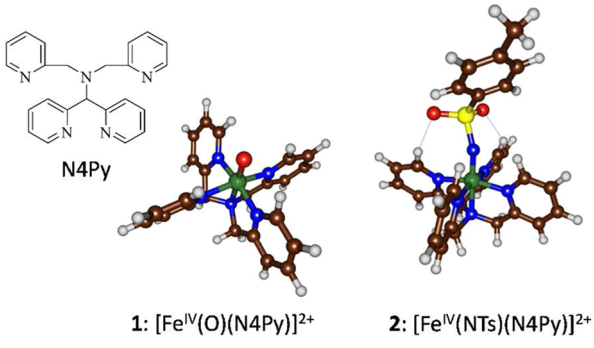

Figure 1. Iron(IV)-oxo and iron(IV)-tosylimido complexes studied in this work.

METHODS

Materials. All chemicals were obtained at the best available purity from Aldrich Chemical Co. and used as specified. Solvents were dried according to published procedures and distilled under argon prior to use.[16] Iodosylbenzene (PhIO) and *N*-tosyliminophenyliodinane (PhINTs) were prepared following literature procedures.[17] Iron(II) complex $[Fe^{II}(N4Py)](CF_3SO_3)_2$ was prepared in a glovebox as reported before.[18] Iron(IV) complexes, $[Fe^{IV}(O)(N4Py)]^{2+}$ and $[Fe^{IV}(NTs)(N4Py)]^{2+}$, were synthesized at ambient temperatures in acetonitrile by reacting the corresponding iron(II) complex with PhIO and PhINTs, respectively.[14,19] The oxidants (**1** and **2**) were characterized with UV−vis spectrophotometry and electrospray ionization mass spectrometry (ESI-MS) methods that confirmed their purity, see Figures S1 and S2 (Supporting Information).[15,19b] Benzyl alcohol-d_7 ($C_6D_5CD_2OH$) was purchased from C/D/N Isotopes Inc. (Pointe-Claire, Quebec, Canada).

Instrumentation. UV−vis spectra and kinetic measurements were recorded on a Hewlett-Packard 8453 spectrophotometer equipped with either a constant temperature circulating water bath or a liquid nitrogen cryostat (Unisoku) with a temperature controller. High resolution ESI-MS spectra of $[Fe^{IV}(O)(N4Py)]^{2+}$ and $[Fe^{IV}(NTs)(N4Py)]^{2+}$ were recorded on a Waters (Micromass MS Technologies) Q-TOF Premier mass spectrometer by infusing precooled (233 K) samples directly into the source at 15 μL min^{-1} using a syringe pump. The spray voltage was set at 2 kV, and the capillary temperature was set at 80 °C. Product analysis was done using NMR (^1H and ^{13}C), whereby the spectra were recorded with a Varian 400/100 MHz spectrometer and LCMS with WATERS ACQUITY UPLC equipped with a variable wavelength UV-200 detector.

Reactivity Studies. All reactions were run in a 10 mm path length UV cuvette by monitoring the UV−vis spectral changes of reaction solutions. Rate constants were determined by fitting the changes in absorbance of the intermediates under study. Their values were measured in triplicate and averaged, which gave a standard deviation of less than 10% of the given values.

Computation. The studies presented in this work use density functional theory (DFT) methods as implemented in the *Jaguar* 7.9 and *Gaussian*-09 program packages.[20] Calculations were performed on $[Fe^{IV}(O)(N4Py)]^{2+}$ (**1**) and $[Fe^{IV}(NTs)(N4Py)]^{2+}$ (**2**) as shown in Figure 1, and their reactivity patterns with 1,3-cyclohexadiene (CHD), benzyl alcohol (BA), and dimethylsulfide (DMS) as model substrates for hydrogen atom abstraction and sulfoxidation processes were investigated. Although calculations have been reported on the reaction mechanism of $[Fe^{IV}(NTs)(N4Py)]^{2+}$ with CHD and DMS,[15] those studies were based on gas-phase geometry optimizations and the effect of solvent was only treated at the single point level. However, because our chemical systems are multiply charged ions, we repeated all studies, whereby full geometry optimizations were performed using a solvent model (polarized continuum model) included that mimics an acetonitrile solution.[21]

Because the spin state ordering of transition metal complexes occasionally varies with the density functional method in the calculations,[22] we tested geometry optimizations with a range of DFT functionals, but all methods converged to very similar spin state orderings and relative energies. Initial studies utilized the unrestricted hybrid density functional method UB3LYP[23] in combination with a double-ζ quality LACVP basis set on iron and 6-31G on the rest of the atoms, basis set BS1.[24] With UB3LYP/BS1, the full potential energy

dx.doi.org/10.1021/ja508403w | J. Am. Chem. Soc. 2014, 136, 17102−17115

landscape from reactants to products on all possible low-lying spin and electronic states was investigated, and local minima and transition states were characterized. Furthermore, intrinsic reaction coordinate scans established the connectivity of the reactants with products via transition states. An analytical frequency calculation at this level of theory confirmed the structures as local minima (with real frequencies only) or first-order saddle points with a single imaginary frequency for the correct mode.

Subsequently all local minima and transition states were reoptimized with a triple-ζ quality basis set that contains an LACV3P+ basis set on iron coupled to 6-311+G* on the rest of the atoms, BS2. To test the reliability of the density functional method, we ran a series of single point calculations at the UB3LYP optimized structures using B3LYP-D3,[25] BP86,[26] PBE0,[27] and M06.[28] These studies did not change the spin state ordering (see Supporting Information) and confirmed the reactivity patterns and the conclusions drawn here.

Kinetic isotope effects (KIEs) were calculated using two models, namely, the semiclassical Eyring model (KIE_E) and the Wigner model (KIE_W), which includes tunneling corrections.[29] KIEs for the hydrogen atom abstraction step of substrates were evaluated from the frequency calculations, whereby the analytical frequencies of the reactants and transition states were recalculated with one or more of the hydrogen atoms of the substrate replaced by deuterium atoms. This led to a change in free energy of activation ($\Delta G^{\ddagger}$) for the original substrate versus that of the deuterium substituted one. The rate constant ratio (k_H/k_D) is then equal to the Eyring KIE, KIE_E, at a specific temperature T (298 K) via eq 1. Further corrections for tunneling are included in the Wigner KIE, KIE_W, which multiplies the KIE_E with the tunneling correction Q_{tH}/Q_{tD}, eqs 2 and 3. In eqs 1−3, R is the gas constant, h is Planck's constant, k_B is the Boltzmann constant, and ν is the imaginary frequency in the transition state.

$$KIE_E = k_H/k_D = \exp[(\Delta G_D^{\ddagger} - \Delta G_H^{\ddagger})/(RT)] \quad (1)$$

$$KIE_W = KIE_E Q_{tH}/Q_{tD} \quad (2)$$

$$Q_t = 1 + \frac{1}{24}\left(\frac{h\nu}{k_B T}\right)^2 \quad (3)$$

The free energy of activation for electron transfer ($\Delta G_{ET}^{\ddagger}$) was calculated using previously described methods,[30] from the driving force for the electron transfer reaction (ΔG_{ET}) and the solvent reorganization energy, λ_0, via eqs 4 and 5. These equations use Avogadro's number (N_A), the elementary charge (e), and the permittivity of vacuum (ε_0). The static and optical dielectric constants (ε_s and ε_{op}) were taken from the Gaussian calculation and had values of 35.688 (acetonitrile) and 1.807, respectively. The hard sphere radii (in Å) of the donor and acceptor molecules of the electron are labeled with r_1 and r_2.

$$\Delta G_{ET}^{\ddagger} = \frac{\lambda_0}{4}\left(1 + \frac{\Delta G_{ET}}{\lambda_0}\right)^2 \quad (4)$$

$$\lambda_0 = \frac{N_A e^2}{4\pi\varepsilon_0}\left(\frac{1}{\varepsilon_{op}} - \frac{1}{\varepsilon_s}\right)\left(\frac{1}{2r_1} + \frac{1}{2r_2} - \frac{1}{r_1 + r_2}\right) \quad (5)$$

RESULTS AND DISCUSSION

Experiment. The reactivity of high valent iron(IV)−oxo complexes has been extensively studied over the past few decades,[2,9,31] but, by contrast, only very few studies have been reported on its closely related iron(V)−nitrido ($Fe^{V}{\equiv}N$) or the iron(IV)−imido ($Fe^{IV}{=}NR$) species. The origin and chemical details of the reaction mechanism of iron(IV)-oxo compared with iron(IV)-imido with substrates are poorly understood; therefore, we decided to do a comparative kinetics study on the two complexes. Two of the most common reaction mechanisms found for enzymatic iron(IV)-oxo intermediates include hydrogen atom abstraction (HAT) and heteroatom oxidation; therefore, we studied the reactivity of **1** and **2** with *para*-X-benzyl alcohol and fluorene as models for HAT and *para*-X-thioanisole as models for heteroatom oxidation.

Complexes **1** and **2** were generated in an acetonitrile solution *in situ*, and subsequently substrate was added. Upon addition of substrate to a solution of **1** and **2**, the intermediates decayed by pseudo-first-order kinetics and the d−d transitions were monitored in the UV−vis spectrum (Figure 2a). The first-order rate constants were then plotted as a function of substrate concentration to obtain the second-order rate constants (k_2) of which we show the example for *para*-H-benzyl alcohol in Figure 2b. Table 1 summarizes the thus obtained second-order rate constants for all substrates discussed here.

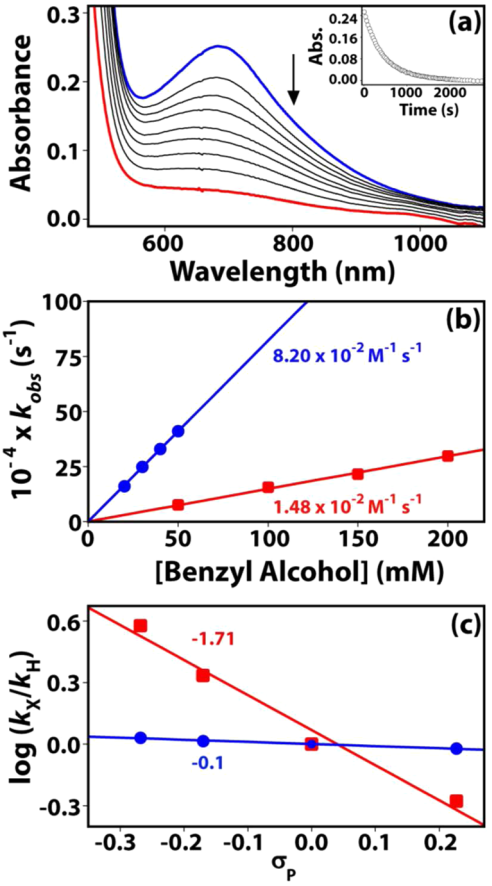

Figure 2. (a) UV−vis spectral changes of **2** (1 mM, blue line) upon the addition of *para*-H-benzyl alcohol (150 equiv diluted in 50 μL of CH_3CN) at 298 K. Inset shows decay profile of 660 nm band. (b) Second-order rate constants determined in the reactions of 1 mM of **1** (●) and **2** (■) in CH_3CN solution against various concentrations of benzyl alcohol at 298 K. (c) Plot of $\log(k_X/k_H)$ against σ_p values of *para*-X-benzyl alcohol in reaction with **1** (●) and **2** (■) at 298 K. The k_X and k_H are the second order rate constants of *para*-X-benzyl alcohol at 298 K.

The second-order rate constant, k_2, obtained for benzyl alcohol at 25 °C was determined to be 1.48×10^{-2} M^{-1} s^{-1} for $[Fe^{IV}(NTs)(N4Py)]^{2+}$, whereas a value of 8.20×10^{-2} M^{-1} s^{-1} was found for $[Fe^{IV}(O)(N4Py)]^{2+}$. Therefore, the $[Fe^{IV}(O)(N4Py)]^{2+}$ complex reacts with benzyl alcohol with rate

dx.doi.org/10.1021/ja508403w | J. Am. Chem. Soc. 2014, 136, 17102−17115

Table 1. Second-Order Rate Constants for the Reaction of 1 and 2 with Selected Substrates

	1			2		
substrate	k_2 (M^{-1} s^{-1})	KIE	Hammett (ρ)	k_2 (M^{-1} s^{-1})	KIE	Hammett (ρ)
thioanisole[a,b]	5.00×10^{-2}		−0.87	2.60×10^{-1}		−3.35
fluorene[b,c]	6.97×10^{-1}	30		1.16×10^{-1}	7	
para-X-benzyl alcohol[c]						
X = OCH_3	8.8×10^{-2}			5.6×10^{-2}		
X = CH_3	8.5×10^{-2}			3.2×10^{-2}		
X = H	8.20×10^{-2}	48[d]	−0.10	1.48×10^{-2}	7	−1.71
X = Cl	7.8×10^{-2}			7.8×10^{-3}		

[a]At 273 K. [b]From ref 15. [c]At 298 K. [d]From ref 32.

constants that are almost six times larger than those found for the $[Fe^{IV}(NTs)(N4Py)]^{2+}$ complex. Similar rate enhancements were found for fluorene, for example, by **1** and **2**.[15] As such the rate enhancement is not dependent on the HAT donor in these cases and most likely proceeds via the same mechanism for both oxidants.

To gain more insight into the details of the hydrogen atom abstraction mechanism, we repeated the experiments with benzyl alcohol-d_7 ($C_6D_5CD_2OH$) and give the comparative second-order rate plots in Figure S6, Supporting Information. These studies established a kinetic isotope effect (KIE) of 7.0, which is relatively low for typical hydrogen atom abstraction reactions but can still be considered as a rate determining HAT step in the reaction mechanism. In the case of HAT of fluorene by **1** and **2**, also a KIE = 7 for the iron(IV)-tosylimido complex was established, whereas a value of 30 was obtained for the iron(IV)-oxo species. Clearly, there are fundamental differences in reactivity between iron(IV)-oxo and iron(IV)-tosylimido that lead to this dramatic lowering of the kinetic isotope effects. Our studies, reported here, are in line with those reported on hydrogen atom abstraction from benzyl alcohol by $[Fe^{IV}(O)(N4Py)]^{2+}$, which also found a large KIE of 48 at 0 °C.[32]

To further understand the intrinsic details of the reaction mechanism of benzyl alcohol with **1** and **2**, we decided to study *para*-substituted benzyl alcohols and create a Hammett plot, see Figure 2c. Reaction of $[Fe^{IV}(O)(N4Py)]^{2+}$ with *para*-substituted benzyl alcohol indicates that the reaction rates are not greatly dependent on the *para*-substituent and whether it is electron-withdrawing or electron-donating gives similar reaction rates. When we plot the reaction rate as a function of σ_p of the substituent, a small Hammett ρ value, approximately −0.1, is found in agreement with the literature.[32] This clearly indicates that there is no substituent effect in the reaction of $[Fe^{IV}(O)(N4Py)]^{2+}$ with benzyl alcohol.

By contrast to the reaction of **1** with benzyl alcohol, the same reaction with **2** gives a dramatic change in substituent effect with a Hammett ρ value of approximately −1.71. This large Hammett value indicates that during the hydrogen atom abstraction from the substrate, there is a considerable amount of positive charge built-up in the transition state. Most likely it originates from additional stabilization of positive charge on the substrate in the transition state by electron-donating groups in the *para*-position of benzyl alcohol and thereby enhances the overall rate of oxidation. The large Hammett value and low KIE indicates that there is a large amount of charge transfer in the rate-determining step.[33]

To unequivocally establish that the rate-determining step is indeed one-electron transfer, we did a subsequent set of experiments with cyclobutanol as mechanistic probe. It has been shown previously that the oxidation of cyclobutanol proceeds through either an initial one-electron or two-electron transfer process, which leads to different products.[32,34] Thus, the one-electron transfer reaction is followed by ring-opening of the substrate to give 4-hydroxybutyraldehyde products, whereas the reaction initiated by a two-electron transfer results in the formation of cyclobutanone products. In the oxidation of cyclobutanol by **2**, we observe 4-hydroxybutyraldehyde as the major products; hence the reaction of **2** with aliphatic substrates proceeds via a dominant radical pathway. By contrast, cyclobutanol reacts with **1** to yield cyclobutanone products after a specific C−H bond cleavage.[32] This observation is in agreement with our earlier observation for the oxidation reaction of fluorene by **1** and **2**, where the latter gives 9,9′-bifluorene as the major product, while with the former fluorenone was obtained.[15]

In addition to the HAT mechanism of **1** versus **2** with selected substrates, we also investigated the sulfoxidation or sulfimidation reaction with *para*-X-thioanisole substrates, X = OCH_3, CH_3, H, and Cl.[15] A plot of the logarithm of the rate constant ratio k_X/k_H gave a linear correlation with the σ_p Hammett parameter with a slope of −0.87 for **1** and −3.35 for **2**, which implicated differences in reaction mechanism. This was assigned as a possible group transfer for the reaction of sulfides with $[Fe^{IV}(O)(N4Py)]^{2+}$ and electron transfer for the reaction with $[Fe^{IV}(NTs)(N4Py)]^{2+}$.

Computation. To gain further insight into the chemical differences between **1** and **2** in hydrogen atom abstraction and heteroatom transfer reactions, we decided to do a detailed density functional theory (DFT) study. To this end, we calculated the catalytic reaction mechanism of hydrogen atom abstraction from 1,3-cyclohexadiene (CHD) and benzyl alcohol (BA) by these oxidants as well as the reaction of **1** and **2** with dimethylsulfide (DMS). Full details of the calculations and the benchmarking of the computational methods are given in the Supporting Information, while we focus on the major trends in the paper here.

Before we discuss the substrate activation by **1** and **2**, let us first do an in-depth analysis of the reactant complexes with and without substrate. Figure 3 displays optimized geometries of $[Fe^{IV}(O)(N4Py)]^{2+}$ (**1**) and $[Fe^{IV}(NTs)(N4Py)]^{2+}$ (**2**) in the lowest lying singlet, triplet, and quintet spin states as obtained after a geometry optimization in a polarized continuum model. In both systems, the triplet spin state is the ground state by more than 4 kcal mol^{-1} over the nearest singlet and quintet spin states.

Optimized geometries of ^{1,3,5}**1** are similar to structures reported previously for gas-phase optimized structures and also to analogous iron(IV)-oxo intermediates from the literature.[35,36] Dramatic geometric differences are found between **1** and **2**. In particular, the Fe−O distance is short, about 1.65−

dx.doi.org/10.1021/ja508403w | J. Am. Chem. Soc. 2014, 136, 17102−17115

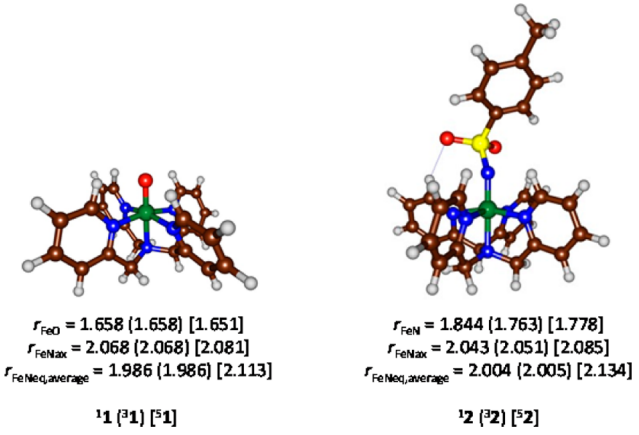

Figure 3. UB3LYP optimized geometries in a dielectric constant mimicking acetonitrile of **1** and **2** with bond lengths in angstroms. The distance between the iron and amide nitrogen atom is labelled as r_{FeNax}, whereas $r_{FeNeq,average}$ represents the average distance of the four iron-pyridine interactions.

1.66 Å in all spin states, typical for a double bond. By contrast, much longer Fe−N bonds are found for structure **2** that range from 1.763 Å for ^{3}**2** to 1.844 Å for ^{1}**2**. Similar bond lengths were obtained from a gas-phase geometry optimization.[15] Despite these differences, structures **1** and **2** have the same electronic configuration with orbital occupation of $\pi^*_{xy}{}^2\pi^*_{xz}{}^1\pi^*_{yz}{}^1$ in the triplet spin state. However, the interactions of the NTs group with the metal differs from that of an oxo group with the metal, and as a result changes in orbital energy levels, orbital ordering, and orbital stability is found.

Figure 4 displays the orbital energy levels of the π^*_{xy}, π^*_{xz}, π^*_{yz}, $\sigma^*_{z^2}$ and $\sigma^*_{x^2-y^2}$ molecular orbitals of ^{3}**1** and ^{3}**2**. The π^*_{xy} orbital is the lowest in energy typical for hexacoordinated iron complexes and its lobes are placed between the nitrogen atoms of the N4Py ligand. However, because the pyridine ligands are orthogonal to the four Fe−N axes, the equatorial nitrogen atoms can still form bonding and antibonding overlap interactions of $2p_x/2p_y$ orbitals with the $3d_{xy}$ orbital on the metal, and hence the π^*_{xy} orbital is higher in energy than in corresponding porphyrin complexes.

The $3d_{xz}$ and $3d_{yz}$ atomic orbitals on Fe interact with a pair of $2p_x/2p_y$ atomic orbitals on the oxo group and form a degenerate pair of π_{xz}/π^*_{xz} and π_{yz}/π^*_{yz} molecular orbitals in **1**. In $[Fe^{IV}(NTs)(N4Py)]^{2+}$, by contrast, the donating nitrogen atom also binds the tosyl group, and as a consequence, the π^*_{xz} and π^*_{yz} are not degenerate anymore. As seen in Figure 4, the $3d_{xz}$ orbital on Fe interacts with the σ_{SN} bonding orbital along the S−N bond to form the π_{xz}/π^*_{xz} set of orbitals, whereas the

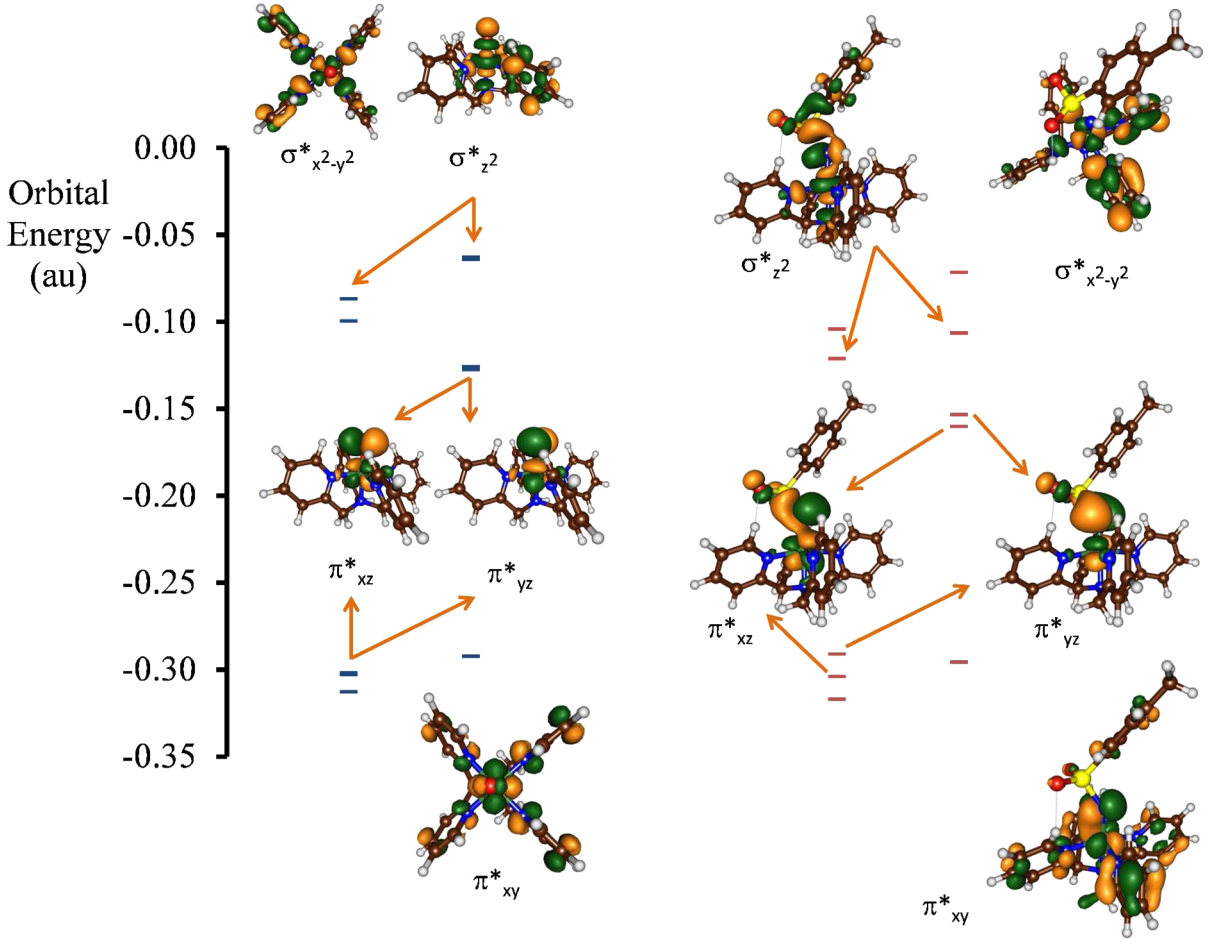

Figure 4. Orbital diagram of $[Fe^{IV}(O)(N4Py)]^{2+}$ (**1**) on the left-hand-side and $[Fe^{IV}(NTs)(N4Py)]^{2+}$ (**2**) on the right-hand-side. The energy levels of the α- and β-set of molecular valence orbitals are given (with energies in au) of both complexes. Also shown are orbital drawings of the relevant molecular orbitals.

dx.doi.org/10.1021/ja508403w | J. Am. Chem. Soc. 2014, 136, 17102−17115

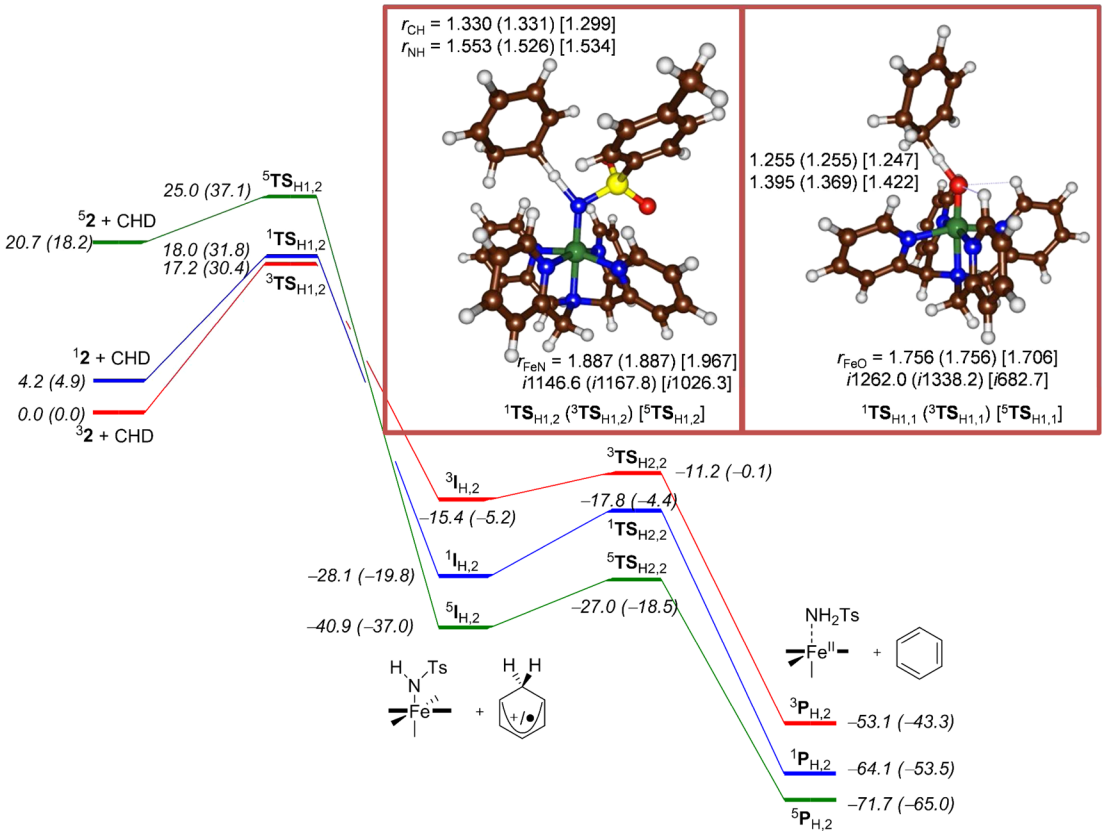

Figure 5. Potential energy landscape of dehydrogenation of CHD by $[Fe^{IV}(NTs)(N4Py)]^{2+}$ with energies relative to isolated reactants in kcal mol^{-1}. Out of parentheses are given ΔE + ZPE values in solvent, whereas free energies with solvent and entropic and thermal corrections are given in parentheses. Also shown are optimized geometries of $\mathbf{TS}_{H1,1}$ and $\mathbf{TS}_{H1,2}$ with bond lengths in angstroms and the imaginary frequency in wave numbers.

$3d_{yz}$ orbital pairs up with a lone pair ($2p_y$) on the nitrogen atom to form π_{yz}/π^*_{yz}.

Two virtual orbitals, $\sigma^*_{z^2}$ and $\sigma^*_{x^2-y^2}$, complement the set of valence orbitals in Figure 4. The $\sigma^*_{x^2-y^2}$ orbital is in the plane of the N4Py ligand and is similar in shape and orbital energy in **1** and **2**. The major orbital differences between **1** and **2** are found along the Fe–O/Fe–N axis. Thus, the $\sigma^*_{z^2}$ molecular orbital for the antibonding interactions of the $3d_{z^2}$ atomic orbital on Fe with the $2p_z$ orbital on O/N is affected strongly.

In **1**, the $\sigma^*_{z^2}$ orbital in $[Fe^{IV}(O)(N4Py)]^{2+}$ is the result of the interaction of the $3d_{z^2}$ orbital on iron with the $2p_z$ atomic orbital on oxygen. By contrast, the $\sigma^*_{z^2}$ orbital in $[Fe^{IV}(NTs)(N4Py)]^{2+}$ is built up from the $3d_{z^2}$ orbital on iron with the $2p_y$ orbital on nitrogen but also includes the $3p_z$ orbital on sulfur. These differences in molecular orbital interactions of the $\sigma^*_{z^2}$ orbital in **1** and **2** affect the energy level dramatically and change the ordering of $\sigma^*_{x^2-y^2}$ over $\sigma^*_{z^2}$, whereby the latter is lower in energy in **2**. The changes in orbital energies affect the HOMO–LUMO gaps, which are reduced in **2** with respect to **1** and thereby increase the electrophilicity of **2** as well. As such, based on the orbital diagrams, differences in chemical reactivity are expected between **1** and **2**.

Hydrogen Atom Abstraction Mechanisms. We then calculated the dehydrogenation of CHD by **1** and **2** with DFT methods, as well as the hydrogen atom abstraction of benzyl alcohol (Supporting Information). As an example of a typical potential energy profile of C–H activation by iron(IV)-tosylimido complexes, we display the dehydrogenation of CHD by ^{1,3,5}**2** in Figure 5. The reaction is stepwise with an initial hydrogen atom abstraction via a transition state $\mathbf{TS}_{H1}$ to form a radical intermediate $\mathbf{I}_H$. A second hydrogen atom abstraction then via transition state $\mathbf{TS}_{H2}$ gives dehydrogenated products, that is, benzene and water/H_2NTs. The labels in superscript refer to the spin multiplicity and the subscript label to the reactant, that is, either **1** or **2**. Thus, $^3\mathbf{TS}_{H1,1}$ is the initial hydrogen atom abstraction transition state from CHD by **1** on the triplet spin state surface.

Note that in the case of the iron(IV)-tosylimido system, actually the reaction starts with an electron transfer from substrate to oxidant prior to the hydrogen atom abstraction. Therefore, we first estimated the electron transfer barrier for reaction 6 using the Marcus equation described with eq 4 above. We estimate the electron transfer free energy of activation ($\Delta G^{\ddagger}_{ET}$) to be 3.4 kcal mol^{-1}, and hence it is well lower than the hydrogen atom abstraction barrier. Note that long-range electron transfer of high-valent iron(IV)-oxo complexes has been calculated before in the reaction of $[Fe(O)(BQEN)(NCCH_3)]^{3+}$, BQEN = *N*,*N*′-dimethyl-*N*,*N*′-bis(8-quinolyl)ethane-1,2-diamine, in a reaction with ethylbenzene as well as in a reaction of Cpd I of P450 with an arginine substrate.[37]

$$^3\mathbf{2} + \text{CHD} \rightarrow [Fe^{III}(NTs)(N4Py)]^+ + \text{CHD}^{\bullet+} + \Delta G_{ET} \quad (6)$$

The initial hydrogen atom abstraction barrier, $\mathbf{TS}_{H1}$, is rate determining in all cases and leads to very stable intermediates $\mathbf{I}_H$ with large exothermicity. The lowest lying barrier, $\mathbf{TS}_{H1,2}$, is on the triplet spin state surface with an energy of $\Delta E^{\ddagger}$ + ZPE =

dx.doi.org/10.1021/ja508403w | J. Am. Chem. Soc. 2014, 136, 17102–17115

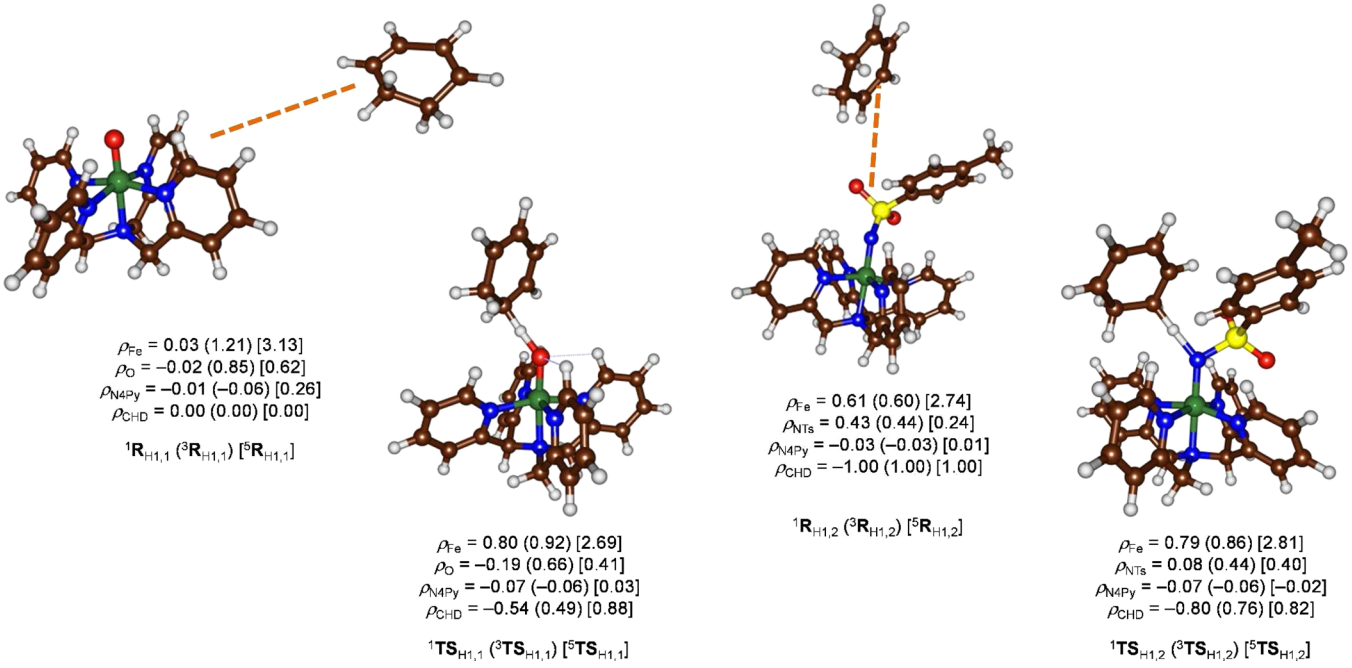

Figure 6. Group spin densities of $\mathbf{R}_{H1,1}$, $\mathbf{TS}_{H1,1}$, $\mathbf{R}_{H1,2}$, and $\mathbf{TS}_{H1,2}$ as obtained at UB3LYP/BS2 in a dielectric constant of 35.688.

17.2 kcal mol^{-1}. By contrast, the reaction of ^{3}**1** with CHD has a hydrogen atom abstraction barrier of 15.7 kcal mol^{-1} at the same level of theory (Supporting Information, Table S31). A change in enthalpy of 1.5 kcal mol^{-1} between the reaction of CHD with **1** and of CHD with **2** leads to a rate enhancement of about 11, which compares well with the one reported experimentally of 6 for *para*-H benzyl alcohol (Table 1), as well as with our previously reported reaction rates for CHD and fluorene.[15]

Although the absolute error of DFT calculated barrier heights is typically several kcal mol^{-1},[38] actually extensive reactivity trends showed that the error is mostly systematic. Thus, for a series of oxygen atom transfer reactions from Cpd I of P450 to substrates, a linear correlation was found with the strength of the C−H bond broken (in the case of HAT) or the ionization potential of the olefin (for epoxidation reactions) with a standard deviation of less than 2 kcal mol^{-1}.[39] Furthermore, DFT calculations on the reaction of ^{4,2}Cpd I with *trans*-2-phenylmethylcyclopropane gave a mixture of rearrangement and nonrearrangement pathways, which enabled the calculation of product isotope effect.[40] The calculated product isotope effect of 1.11 was very close to the experimental value of 1.14; hence DFT can calculate small regioselectivity differences of a few kcal mol^{-1} with good accuracy.

Past the transition state, $\mathbf{TS}_{H1,2}$, a spin crossing to a higher spin state occurs to form $\mathbf{I}_{H,2}$ in the quintet spin state. In the transition state, however, the triplet is well below the quintet spin. With iron(IV)-oxo as an oxidant, the second hydrogen atom abstraction has negligible barriers, but for [Fe^{IV}(NTs)(N4Py)]$^{2+}$, significant barriers, for example, ΔE + ZPE = 13.9 kcal mol^{-1} for $^{5}\mathbf{TS}_{H2,2}$, are found. This will imply that the radical intermediates have a finite lifetime during which rearrangement processes may occur leading to side reactions and byproducts.[41]

Geometrically, $\mathbf{TS}_{H1,1}$ is different from $\mathbf{TS}_{H1,2}$, although the value of the imaginary frequency is of the same order of magnitude. In particular, the N−H bond in $\mathbf{TS}_{H1,2}$ is rather long with values well over 1.5 Å, whereas the O−H distance in $\mathbf{TS}_{H1,1}$ is between 1.369 and 1.422 Å for the three spin states. Optimized geometries of intermediates and products are in line with previous studies on dehydrogenation processes by iron(IV)-oxo and iron(IV)-tosylimido complexes.[42,43]

To understand the differences between $\mathbf{TS}_{H1,1}$ and $\mathbf{TS}_{H1,2}$, we plot in Figure 6 the group spin densities of these transition states as well as the reactant complexes. At first glance, the two sets of spin densities for the transition states look very similar: In the triplet spin state there is about 1.5 spin density on the FeO/FeNTs group and considerable radical character on the substrate. However, a careful look at the reactant complexes $\mathbf{R}_{H1,1}$ and $\mathbf{R}_{H1,2}$ shows that the iron(IV)-tosylimido complex has undergone an electron transfer upon approach of the substrate, and $^{1,3,5}\mathbf{R}_{H1,2}$ all show a spin density of approximately 1 at the CHD unit. This may affect the spin densities and charge distributions in the transition states as well.

The group spin densities of the iron(IV)-oxo species in ^{1,3,5}**1** and $^{1,3,5}\mathbf{R}_{H1,1}$ are very similar, and little spin density has accumulated on the substrate moiety in $\mathbf{R}_{H1,1}$. Therefore, approach of the substrate on the iron(IV)-oxo species has little effect on the charge distributions, and in $\mathbf{R}_{H1,1}$ the oxidant is still an iron(IV)-oxo species. A comparison of the group spin densities of ^{1,3,5}**2** and $^{1,3,5}\mathbf{R}_{H1,2}$, on the other hand, shows that an electron transfer has occurred at relatively large distance and in $\mathbf{R}_{H1,2}$ the metal is reduced and the substrate is a cation radical, that is, [Fe^{III}(NTs)(N4Py)]$^{+}$···CHD$^{+\bullet}$ rather than [Fe^{IV}(NTs)(N4Py)]$^{2+}$···CHD. Hence the actual oxidant that performs the hydrogen atom abstraction is the iron(III)-tosylimido species rather than an iron(IV)-tosylimido species. Because experimental rate constants were measured after addition of substrate, this implies that we cannot use the reactant complex $\mathbf{R}_{H1,2}$ as a comparison with experiment but have to use isolated reactants instead. Clearly, the electron affinity of [Fe^{IV}(NTs)(N4Py)]$^{2+}$ is large, and the electron transfer happens prior to the substrate activation step. In recent work, we showed that binding of Zn^{2+} to a manganese-porphyrinoid system resulted in valence tautomerism and changes in electronic configuration

Scheme 1. Reaction Mechanisms Established for Iron(IV)-oxo and Iron(IV)-tosylimido Complexes

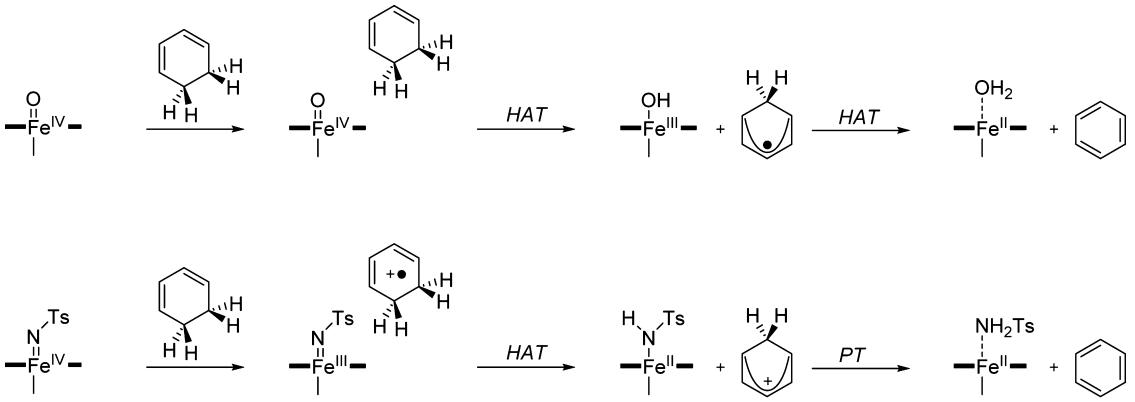

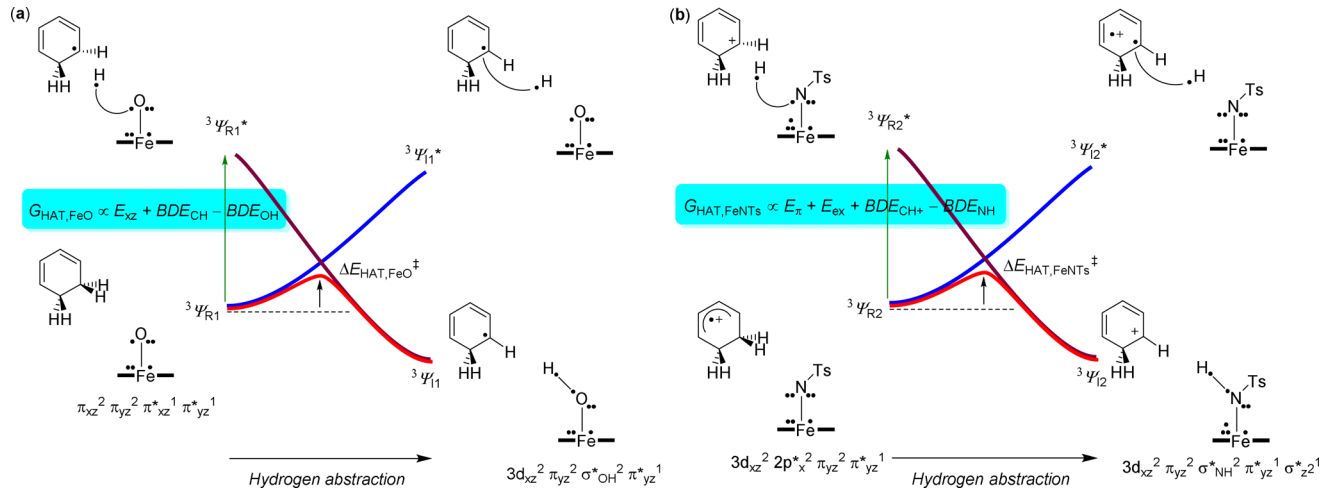

Figure 7. Valence bond curve crossing diagrams for hydrogen atom abstraction from substrate by $[Fe^{IV}(O)(N4Py)]^{2+}$ (a) and $[Fe^{III}(NTs)(N4Py)]^{+}$ (b). Valence electrons are identified with a dot, and lines (straight or bent) in chemical structures refer to bonds.

and consequently catalysis.[44] The $[Fe^{IV}(NTs)(N4Py)]^{2+}$ system, therefore, is another example of a catalyst where its activity is strongly dependent on environmental variables.

Note that the spin densities on the quintet spin state surface for $\mathbf{R}_{H1,2}$ and $\mathbf{TS}_{H1,2}$ implicate the ferromagnetic coupling of three electrons on iron with one on the substrate rest group. Previous studies on nonheme iron(IV)-oxo reactivity[35,36] found quintet spin states with five unpaired electrons on the iron(IV)-oxo antiferromagnetically coupled to a radical on the substrate rest group as the most stable radical intermediate. In these systems, the hydrogen atom typically attacks from the top and aligns itself with the Fe−O axis. In iron(IV)-tosylimido, this site is blocked by the tosylimido group, and the substrate attacks along an angle, thus stabilizing the π-pathway. We made attempts to swap molecular orbitals and create alternative quintet spin states with five unpaired electrons on the metal antiferromagnetically coupled to a substrate radical for transition states and intermediate complexes. However, all these calculations failed and led to high energy structures only.

The group spin densities and, in particular, the differences between $\mathbf{R}_{H1,1}$ and $\mathbf{TS}_{H1,1}$ and between $\mathbf{R}_{H,2}$ and $\mathbf{TS}_{H1,2}$ show that in both cases between the reactant complex and the **TS** a hydrogen atom abstraction takes place. The differences between the two processes are that in the iron(IV)-tosylimido already one electron had transferred upon formation of a long-range complex **R**, thereby generating a triplet ground state with $\pi^*_{xy}{}^2\pi^*_{xz}{}^2\pi^*_{xz}{}^1\pi_{CHD}{}^1$ configuration representing a state corresponding to $[Fe^{III}(NTs)(N4Py)]^{+}\cdots CHD^{+\bullet}$. Therefore, the subsequent hydrogen atom abstraction includes a second electron to be transferred and the formation of a $[Fe^{II}(NHTs)(N4Py)]$ intermediate. This complex then abstracts a proton to form the product complex. The $^3\mathbf{TS}_{H1,2}$ structure, therefore, has an electronic configuration closely resembling the product complexes, where the aromaticity in the benzene group is starting to form and an electron transfer from substrate into $\sigma^*_{z^2}$ takes place.

The singlet spin state reactant complex has the same electronic configuration as $^3\mathbf{R}_{H1,2}$, and its transition state is very close in energy to $^3\mathbf{TS}_{H1,2}$ and leads through an electron transfer to the closed-shell singlet intermediate $^1\mathbf{I}_{H,2}$ with configuration $\pi^*_{xy}{}^2\pi^*_{xz}{}^2\pi^*_{yz}{}^2$. The most stable intermediate, however, is $^5\mathbf{I}_{H,2}$ with configuration $\pi^*_{xy}{}^2\pi^*_{xz}{}^1\pi^*_{yz}{}^1\sigma^*_{z^2}{}^1\sigma^*_{x^2-y^2}{}^1$. Scheme 1 summarizes the mechanisms that we obtained for dehydrogenation of olefins, such as CHD, by **1** and **2**. The $\sigma^*_{z^2}$ orbital in $^3\mathbf{TS}_{H1,2}$ mixes strongly with a π-orbital on the aromatic substrate and hence is strongly affected in shape and energy level by the *para*-substituent on the ring. We can anticipate a large Hammett effect upon changing the *para*-H substituent by a more electron donating or withdrawing group.

The reaction mechanisms shown in Scheme 1 also explain the Hammett plot for benzyl alcohol in Figure 2c. Thus, the iron(IV)-oxo complex reacts with little charge accumulation on

dx.doi.org/10.1021/ja508403w | J. Am. Chem. Soc. 2014, 136, 17102−17115

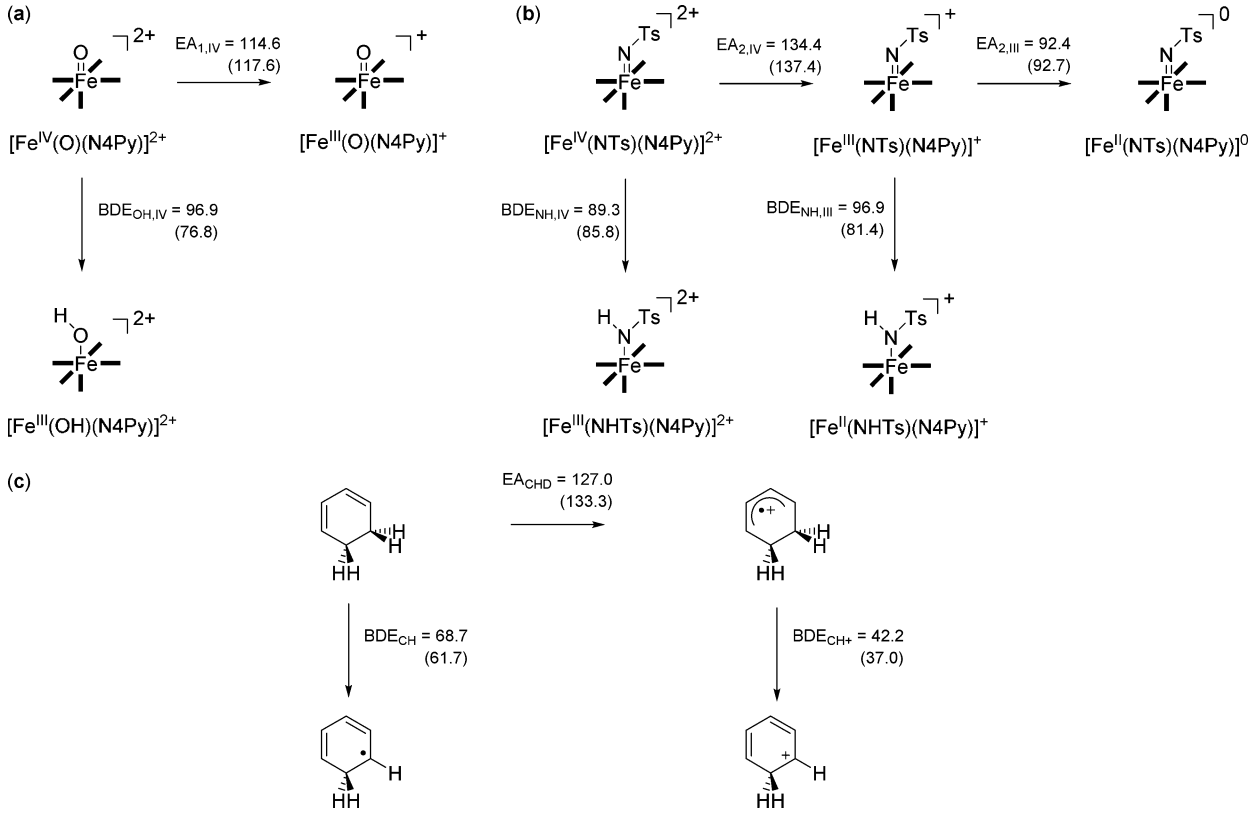

Figure 8. Thermochemical cycles for electron and hydrogen atom transfer from $[Fe^{IV}(O)(N4Py)]^{2+}$ (a), $[Fe^{IV}(NTs)(N4Py)]^{2+}$ (b), and cyclohexadiene (c). All data obtained after a UB3LYP/BS2//UB3LYP/BS1 calculation in a dielectric constant. Data out of parentheses are ΔE + ZPE values in solvent, whereas free energies are in parentheses.

the substrate and hence has an almost zero Hammett ρ value. By contrast, the iron(IV)-tosylimido complex starts the reaction with an electron transfer and the formation of a substrate cation radical. This large charge accumulation on the substrate has a strong effect on the Hammett parameter and as a result a value of $\rho = -1.71$ is obtained.

To further understand the intricate details of HAT reaction mechanisms by $[Fe^{IV}(O)(N4Py)]^{2+}$ versus $[Fe^{IV}(NTs)(N4Py)]^{2+}$, we did a valence bond (VB) and thermochemical analysis on the basic chemical properties of oxidants and substrates. Figure 7 displays the curve crossing diagrams of hydrogen atom abstraction by the reactant complexes $\mathbf{R}_{H1,1}$ and $\mathbf{R}_{H1,2}$. As discussed above, approach of CHD on an iron(IV)-oxo species gives $\mathbf{R}_{H1,1}$ or $[Fe^{IV}(O)(N4Py)]^{2+}\cdots$CHD. However, when CHD approaches the $[Fe^{IV}(NTs)(N4Py)]^{2+}$ complex instead, an electron transfer takes place to form $\mathbf{R}_{H1,2}$ or $[Fe^{III}(NTs)(N4Py)]^{+}\cdots CHD^{+\bullet}$. Figure 7 reflects these starting conditions and discusses the hydrogen atom abstraction mechanism from the reactant complexes.

The valence bond (VB) curve crossing diagrams start at the bottom left with the reactant complexes, that is, $\mathbf{R}_{H1,1}$ or $\mathbf{R}_{H1,2}$, which have a reactant wave function Ψ_{R1} and Ψ_{R2}, respectively. We then consider the hydrogen atom abstraction leading to intermediates $\mathbf{I}_{H1}/\mathbf{I}_{H2}$, which are described on the bottom right-hand-side of the figure with product wave function Ψ_{I1}/Ψ_{I2}. The crossing of the reactant and product wave functions leads to an avoided crossing and a hydrogen atom abstraction barrier with energy $\Delta E^{\ddagger}_{HAT}$. Previously, it has been shown that $\Delta E^{\ddagger}_{HAT}$ is proportional to a fraction of the excitation energy (G) for the excitation from Ψ_R to Ψ_R* in the reactant geometry.[45] In order to understand the factors that determine the actual value of G in the reaction of $[Fe^{IV}(O)(N4Py)]^{2+}$ and $[Fe^{IV}(NTs)(N4Py)]^{2+}$ with CHD, we display the VB structures of the ground and excited states corresponding to the Ψ_R and Ψ_R* wave functions. Note that upon approach of the substrate to $[Fe^{IV}(NTs)(N4Py)]^{2+}$ an electron transfer has taken place; therefore, we use $[Fe^{III}(NTs)(N4Py)]^{+}\cdots CHD^{+\bullet}$ as a reactant configuration instead.

The iron(IV)-oxo complex has electronic configuration $\pi_{xz}{}^2\pi_{yz}{}^2\pi^*_{xy}{}^2\pi^*_{xz}{}^1\pi^*_{yz}{}^1$ in a ground state triplet. The π_{xz}/π^*_{xz} and π_{yz}/π^*_{yz} pair of orbitals are located along the Fe−O bond, and the electrons in these orbitals are identified with dots, while the π^*_{xy} electrons have been omitted from Figure 7 for clarity. Hydrogen atom abstraction splits the π_{xz}/π^*_{xz} pair of orbitals back into atomic orbitals with two electrons in $3d_{xz}$ and a single electron in $2p_x$. The latter electron pairs up with the electron of the incoming hydrogen atom to form a σ_{OH} bond.

A comparison between the VB structures representing Ψ_{R1} and Ψ_{R1}* should give information on the components that affect the excitation energy and consequently the hydrogen atom abstraction barrier. The difference between the two VB structures highlights the breaking of the C−H bond of the substrate, the formation of the O−H bond, and the dehybridization of the π_{xz}/π^*_{xz} pair of orbitals. The excitation energy, $G_{HAT,FeO}$, therefore, includes the energy to break the C−H bond of the substrate, that is, BDE_{CH}, the energy to form an O−H bond, that is, BDE_{OH}, and finally the energy to split the π_{xz}/π^*_{xz} pair of molecular orbitals into atomic orbitals, E_{xz}, eq 7.

$$G_{HAT,FeO} = E_{xz} + BDE_{CH} - BDE_{OH} \quad (7)$$

dx.doi.org/10.1021/ja508403w | J. Am. Chem. Soc. 2014, 136, 17102−17115

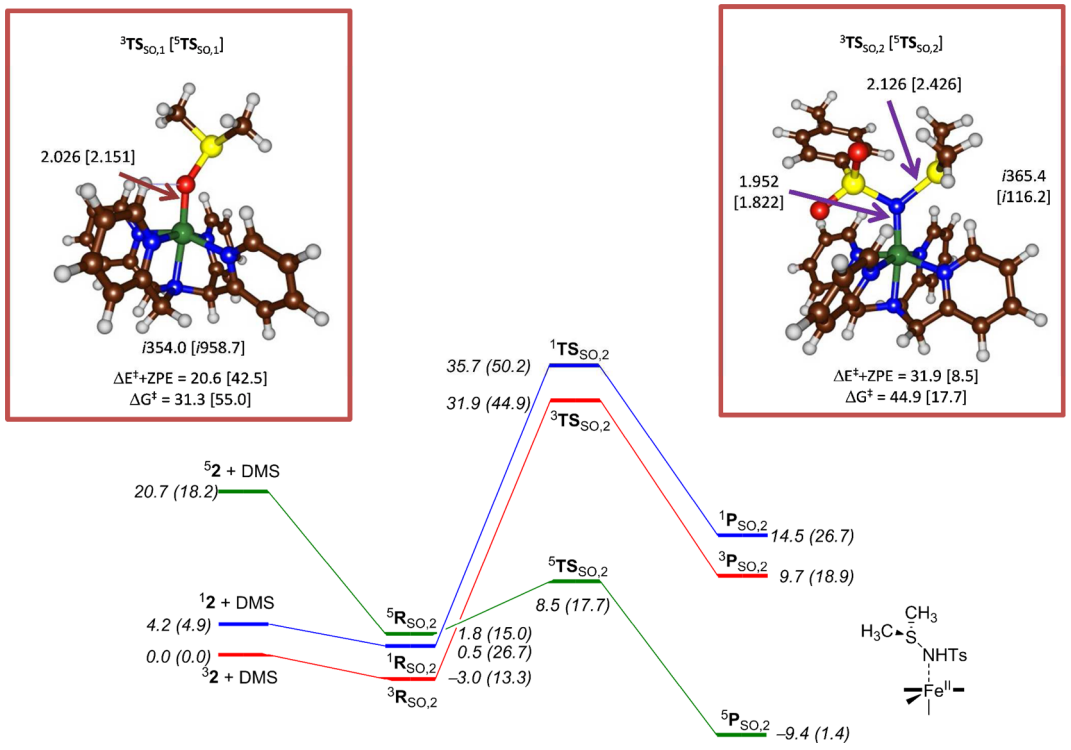

Figure 9. Potential energy landscape of dehydrogenation of CHD by $[Fe^{IV}(NTs)(N4Py)]^{2+}$ with energies relative to isolated reactants in kcal mol^{-1}. Out of parentheses are given ΔE + ZPE values in solvent, whereas free energies with solvent and entropic and thermal corrections are given in parentheses. Also shown are optimized geometries of $\mathbf{TS}_{SO,1}$ and $\mathbf{TS}_{SO,2}$ with bond lengths in angstroms and the imaginary frequency in wave numbers.

The situation is radically different for the reaction of $[Fe^{IV}(NTs)(N4Py)]^{2+}$ with CHD, where prior to the formation of the reactant complex an electron transfer has taken place. Figure 7b, therefore, starts bottom left with the $[Fe^{III}(NTs)(N4Py)]^{+}$ in close approach with CHD cation radical. The reactant wave function for this system is $3d_{xz}^{2}2p_x^{2}\pi_{yz}^{2}\pi^*_{xy}^{2}\pi^*_{yz}^{1}$. In the hydrogen atom abstraction, the C−H bond of the substrate ($CHD^{+\bullet}$) is broken, which will cost BDE_{CH+}. Note that with the iron(IV)-oxo species a hydrogen atom abstraction is from CHD, whereas with the iron(III)-tosylimido group it is from $CHD^{+\bullet}$. The values of BDE_{CH} and BDE_{CH+} are different, *vide infra*.

The hydrogen atom attacks the $2p_x$ orbital and forms a new σ_{NH} bond; however, since there are three electrons in the interaction, one of those is promoted into the $\sigma^*_{z^2}$ orbital, and therefore the bond formation energy is equal to the energy to form the N−H bond, that is, BDE_{NH}, plus the excitation energy from $2p_x$ to $\sigma^*_{z^2}$, E_{ex}. In addition, the radical left behind on the carbon atom, which originally bound the hydrogen atom conjugates with the remaining electrons of the $CHD^{+\bullet}$ π-system with energy E_π, eq 8.

$$G_{HAT,FeNTs} = E_\pi + E_{ex} + BDE_{CH+} - BDE_{NH} \quad (8)$$

To get a feeling for the magnitude of $G_{HAT,FeO}$ versus $G_{HAT,FeNTs}$, we calculated the various bond dissociation energies (BDEs) and ionization energies (IEs) as summarized in the thermochemical cycles in Figure 8. We calculate values ΔE + ZPE of 68.7 kcal mol^{-1} for BDE_{CH} and 96.9 kcal mol^{-1} for BDE_{OH}. The value of E_{xz} in eq 7 is estimated from the energy gap between the π_{xz} and π^*_{xz} α-orbitals in $^3[Fe^{IV}(O)(N4Py)]^{2+}$ for which we find 76.7 kcal mol^{-1}. Therefore, $G_{HAT,FeO}$ is estimated to have a value of 48.5 kcal mol^{-1}. Generally, the barrier height is about one-third of the height of the excitation energy G,[46] which in our case would lead to a VB predicted barrier height of $\Delta E^{\ddagger}_{HAT,FeO}$ = 16.2 kcal mol^{-1} for the reaction between **1** and CHD. The VB predicted barrier matches the DFT calculated one of 15.7 kcal mol^{-1} (Supporting Information, Table S31) perfectly.

Using a similar approach, we estimate the excitation energy $G_{HAT,FeNTs}$: the bond energy of the C−H bond in $CHD^{+\bullet}$ is BDE_{CH+} = 42.2 kcal mol^{-1}, whereas the N−H bond formation energy between $[Fe^{III}(NTs)(N4Py)]^{+}$ and a hydrogen atom is BDE_{NH} = 96.9 kcal mol^{-1} (Figure 8).

The $2p_x \rightarrow \sigma^*_{z^2}$ excitation energy is taken from the difference in energy of these orbitals in $[Fe^{III}(NTs)(N4Py)]^{+}$ and estimated to be 72.9 kcal mol^{-1}. The π-conjugation energy of olefins was previously reported to be about 32 kcal mol^{-1}.[47] As such, a value of $G_{HAT,FeNTs}$ = 50.2 kcal mol^{-1} is predicted from VB theory. A fraction of one-third of this value would give a $\Delta E^{\ddagger}_{HAT,FeNTs}$ = 16.7 kcal mol^{-1} again in good agreement with the DFT calculations reported in Figure 5. Furthermore, the VB estimated barriers reproduce the experimentally observed and DFT calculated ordering.

In conclusion, the VB curve crossing diagrams predict the iron(IV)-oxo species to be more reactive with CHD than the corresponding iron(III)-tosylimido system, because of a large contribution to the excitation energy for $2p_x$ to $\sigma^*_{z^2}$ promotion. Even though the driving force of the reaction for $[Fe^{III}(NTs)(N4Py)]^{+}$ with $CHD^{+\bullet}$ is larger than the one for $[Fe^{IV}(O)(N4Py)]^{2+}$ with CHD as also follows from the differences in BDE values.

The data in Figure 8 also shows that the electron affinity of **2** is considerably larger than that of **1** by about 20 kcal mol^{-1}. As

dx.doi.org/10.1021/ja508403w | J. Am. Chem. Soc. 2014, 136, 17102−17115

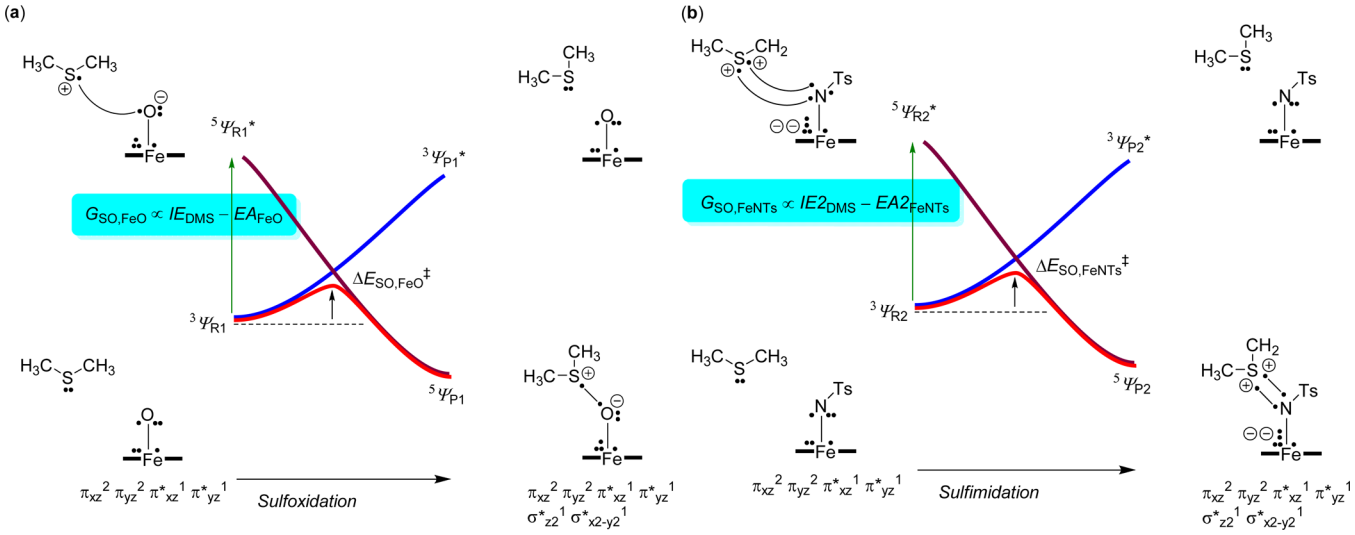

Figure 10. Valence bond curve crossing diagrams for sulfoxidation/sulfimidation from substrate by $[Fe^{IV}(O)(N4Py)]^{2+}$ (a) and $[Fe^{III}(NTs)(N4Py)]^{+}$ (b). Valence electrons are identified with a dot, and lines (straight or bent) in chemical structures refer to bonds.

a result of this, the electron transfer reaction of **1** with CHD is endergonic, whereas it is exergonic with **2**, eqs 9 and 10.

$$\mathbf{1} + \mathrm{CHD} \rightarrow [Fe^{III}(O)(N4Py)]^{+} + \mathrm{CHD}^{+\bullet}$$
$$\Delta G = 15.8\ \mathrm{kcal\ mol^{-1}} \quad (9)$$

$$\mathbf{2} + \mathrm{CHD} \rightarrow [Fe^{III}(NTs)(N4Py)]^{+} + \mathrm{CHD}^{+\bullet}$$
$$\Delta G = -4.1\ \mathrm{kcal\ mol^{-1}} \quad (10)$$

Indeed, a geometry optimization of the reactant complexes $\mathbf{R}_{H1,1}$ and $\mathbf{R}_{H1,2}$ shows that the iron(IV)-tosylimido group is reduced to an iron(III) species, whereas no electron transfer has occurred for the iron(IV)-oxo intermediate. As a consequence, the hydrogen atom abstraction in $\mathbf{TS}_{H1,1}$ is from CHD, whereas it is from $\mathrm{CHD}^{+\bullet}$ in $\mathbf{TS}_{H1,2}$. The C−H bond strength in $\mathrm{CHD}^{+\bullet}$ is considerably weaker than that in CHD by ΔG = 24.7 kcal mol^{-1}, which should lower the barrier as well.

In order to find out whether the thermodynamics and kinetics of eq 10 is affected by the tosyl group bound to the iron(IV)-imido, we decided to calculate the same reaction for $[Fe^{IV}(NCH_3)(N4Py)]^{2+}$ and $[Fe^{IV}(NC_6H_5)(N4Py)]^{2+}$ as possible oxidants. We find free energy values (ΔG with solvent corrections) for eq 10 of 25.1 kcal mol^{-1} for $[Fe^{IV}(NCH_3)(N4Py)]^{2+}$ and 20.1 kcal mol^{-1} for $[Fe^{IV}(NC_6H_5)(N4Py)]^{2+}$. Consequently, the tosylimido group is strongly electron-withdrawing and enables a long-range electron transfer, while this is not possible with the alternative $[Fe^{IV}(NCH_3)(N4Py)]^{2+}$ and $[Fe^{IV}(NC_6H_5)(N4Py)]^{2+}$ complexes.

A HAT reaction of a substrate with **1** or **2** will lead to radical intermediates **I** with a reaction (free) energy equal to the difference in BDE_{CH} and BDE_{NH}/BDE_{OH}. Moreover, often the natural logarithm of the rate constant for HAT also is proportional to either BDE_{CH} or BDE_{OH} as seen in several examples of metal-oxo complexes.[48] Technically, however, the BDE_{OH} value essentially represents an electron and a proton transfer, which do not necessarily transfer to the same place. The BDE_{OH} is described in eq 11 into individual components for the electron affinity (EA), the acidity of the hydroxo group (ΔG_{acid}), and the ionization energy of an isolated hydrogen atom (IE_H).[49]

$$BDE_{OH} = -EA - \Delta G_{acid} - IE_H \quad (11)$$

The ionization energy of a hydrogen atom is 13.598 eV,[50] and together with our reported values of BDE_{OH}/BDE_{NH} and EA from Figure 8, we calculate a ΔG_{acid} = 211.8 kcal mol^{-1} for $[Fe^{IV}(O)(N4Py)]^{2+}$, whereas values of 262.1 and 343.5 kcal mol^{-1} are found for $[Fe^{IV}(NTs)(N4Py)]^{2+}$ and $[Fe^{III}(NTs)(N4Py)]^{2+}$. Thus, based on the acidity values, one would expect the iron(IV)-tosylimido and iron(III)-tosylimido complexes to be much better oxidants of HAT reactions. Indeed, the DFT calculated reaction energy for the HAT reaction is well larger for **2** than it is for **1** in agreement with the relative acidity values. The fact that the barrier heights do not follow this trend is due to stereochemical interactions of the approaching substrate with the bulky tosylimido group. The iron(IV)-oxo group, on the other hand, experiences very little stereochemical interactions with the approaching substrate.

Sulfoxidation Mechanisms. Subsequently, we investigated the sulfoxidation and sulfimidation of dimethylsulfide (DMS) by **1** and **2**, respectively, and the calculated potential energy profile for $[Fe^{IV}(NTs)(N4Py)]^{2+}$ is given in Figure 9, as well as the rate determining transition states for all systems calculated. The collision of DMS with oxidant leads to the formation of a reactant complex $\mathbf{R}_{SO}$, and heteroatom oxidation proceeds via barrier $\mathbf{TS}_{SO}$ to form the product complexes $\mathbf{P}_{SO}$. In both sets of calculations, the substrate approaches the oxidant from the side and reacts in a concerted pathway by insertion of the sulfide into the O/N system. Optimized geometries of the transition states give an FeN−SMe_2 distance that is only slightly longer than the FeO−SMe_2 distance, and in both cases it is longer in the quintet than in the triplet spin state.

The imaginary frequencies found for the $\mathbf{TS}_{SO}$ barriers are significantly lower than the ones reported above for the hydrogen atom abstraction barriers because heavier atoms are involved in the motion. The geometries and imaginary frequencies are in good agreement with previous substrate sulfoxidation transition states from the literature.[51]

In both chemical systems, the product complexes are most stable in the quintet spin state, whereas reactants (**1** and **2**) have a triplet spin ground state. This indicates that a spin crossover from triplet to quintet will need to take place on the potential energy surface during the course of the reaction. In

dx.doi.org/10.1021/ja508403w | J. Am. Chem. Soc. 2014, 136, 17102−17115

the sulfimidation reaction, the quintet spin transition state is well below the triplet in energy ($\Delta G^{\ddagger}$ = 17.7 kcal mol^{-1} for ^{5}**TS**$_{SO,2}$ and $\Delta G^{\ddagger}$ = 44.9 kcal mol^{-1} for ^{3}**TS**$_{SO,2}$), and consequently the spin state crossing happens well before the sulfimidation barrier.

The opposite is found for the reaction starting with the iron(IV)-oxo species, where ^{3}**TS**$_{SO,1}$ is lower in energy than ^{5}**TS**$_{SO,1}$. Furthermore, the absolute value of the barrier height for sulfoxidation is well higher than the sulfimidation reaction. Therefore, DFT predicts dimethylsulfide to react faster with [Fe^{IV}(NTs)(N4Py)]$^{2+}$ than with [Fe^{IV}(O)(N4Py)]$^{2+}$ in agreement with experimental observation (compare with Table 1).

Note that in the corresponding reactant complexes (**R**$_{SO,1}$ and **R**$_{SO,2}$) no charge transfer has occurred from substrate to oxidant in contrast to the results described in Figure 6 for **R**$_{H,2}$. This implies that the reactivities of **1** as well as the sulfimination by **2** start from an iron(IV) species, whereas the reaction of hydrogen atom abstraction by **2** is performed by its reduced species, that is, [Fe^{III}(NTs)(N4Py)]$^{+}$, and ionized CHD. Because of this difference the reactivity pattern has changed.

To further understand the heteroatom oxidation mechanism by **1** and **2** and to find the origin of the reactivity differences, we developed the corresponding VB curve crossing diagrams (Figure 10). These diagrams are similar to those reported above for the HAT processes but now connect the reactant wave function ($^{3}\Psi_{R}$) with the product wave function ($^{5}\Psi_{P}$) directly in a concerted reaction step. The sulfoxidation by iron(IV)-oxo complexes follows a VB diagram as reported before,[45c,52] whereby essentially a single electron transfer in the transition state for S−O bond formation occurs.

One of the electrons from one of the lone-pairs of the DMS substrate is transferred to the iron (into the $\sigma^{*}_{z^2}$ orbital), and a new S−O bond is formed between the singly occupied orbital on S with the singly occupied 2p$_x$ orbital on oxygen. The corresponding promotion gap for the sulfoxidation of DMS by **1** will, therefore, be proportional to the ionization potential of DMS (IE$_{DMS}$) as well as the electron affinity of **1** (EA$_{FeO}$). Indeed previous studies on trends in substrate sulfoxidation by iron(IV)-oxo complexes showed a linear correlation between the barrier height (**TS**$_{SO}$) and the IE of the substrate.[51c]

In the case of the reaction of DMS with **2**, the orbital occupation and group spin densities in the transition state implicate a double electron transfer and the formation of an electronic state that resembles the product complex. Thus, the double electron transfer with **2** occurs early on the potential energy surface and both electrons are transferred in the **TS**, while with **1** only one electron has moved yet in **TS**$_{SO}$. Because of this, the barrier height according to the VB curve crossing diagram will be dependent on the second ionization potential of DMS (IE2$_{DMS}$) for the removal of two electrons (from both lone pairs on sulfur) from DMS. At the same time, the oxidant accepts two electrons (into $\sigma^{*}_{x^2-y^2}$ and $\sigma^{*}_{z^2}$), and hence the double electron affinity (EA2$_{FeNTs}$) will determine the barrier height. The free energy (ΔG_{solv}) for conversion of [Fe^{IV}(NTs)(N4Py)]$^{2+}$ into [Fe^{III}(NTs)(N4Py)]$^{+}$ is 137.4 kcal mol^{-1} and the subsequent electron abstraction another 92.7 kcal mol^{-1} (Figure 8).

By contrast, the first electron affinity for [Fe^{IV}(O)(N4Py)]$^{2+}$ is 117.6 kcal mol^{-1}, and the addition of a second electron is 74.8 kcal mol^{-1}. Consequently, the two electron abstraction by **2** is 37.7 kcal mol^{-1} more favorable than that by **1**, which makes the two-electron transfer process for the heteroatom oxidation thermochemically favorable for the [Fe^{IV}(NTs)(N4Py)]$^{2+}$ complex, and as a result **TS**$_{SO,1}$ is higher in energy than **TS**$_{SO,2}$. Therefore, the iron(IV)-tosylimido complex will react with higher rate constants with sulfides than the corresponding iron(IV)-oxo complex.

The DFT and VB analyses, therefore, highlight the differences in chemical properties of [Fe^{IV}(NTs)(N4Py)]$^{2+}$ versus [Fe^{IV}(O)(N4Py)]$^{2+}$ that enable differences in reactivity patterns.

CONCLUSIONS

A combined kinetics and computational study is presented on the relative oxidative power of iron(IV)-oxo and iron(IV)-tosylimido. The experimental studies show that the iron(IV)-tosylimido reacts faster in heteroatom oxidation reactions, such as sulfimidation, compared with the iron(IV)-oxo species. However, the opposite trend is found for HAT reactions from, for example, *para*-X-benzyl alcohol and fluorene. Subsequent DFT calculations confirmed the experimentally observed trends and gave smaller barriers for HAT by iron(IV)-oxo complexes relative to iron(IV)-imido, whereas the reverse trend is found for heteroatom transfer. The origin of the rate reversal was investigated through a thermochemical analysis of the bond breaking and electron transfer processes. It was found that the electron affinity of [Fe^{IV}(NTs)(N4Py)]$^{2+}$ is so high that it accepts electrons from HAT substrates at a large distance, which was due to differences in orbital interactions compared with the iron(IV)-oxo species. As a result of that, the actual HAT is performed by its reduced species, that is, [Fe^{III}(NTs)(N4Py)]$^{+}$, which is catalytically much less potent than an iron(IV)-oxo species. On the other hand, heteroatom transfer reactions do not start with a long-range electron transfer but proceed via a rate determining group transfer, whereby two-electrons are transferred to the iron(IV)-imido, whereas only one electron is transferred yet at the same point along the potential energy profile in the reaction with the iron(IV)-oxo complex. A thermochemical and valence bond analysis has identified the key components that drive the reaction mechanism and cause a reactivity preference switch from preferred heteroatom transfer for iron(IV)-tosylimido to hydrogen atom transfer for iron(IV)-oxo.

ASSOCIATED CONTENT

Supporting Information

Detailed description of methods and techniques as well as full data of the calculations, including optimized geometries and Cartesian coordinates, as well as tables with group spin densities, group charges, absolute (free) energies, and relative (free) energies. This material is available free of charge via the Internet at http://pubs.acs.org.

AUTHOR INFORMATION

Corresponding Authors

sam.devisser@manchester.ac.uk
dkclcre@yahoo.com
sastricv@iitg.ernet.in

Notes

The authors declare no competing financial interest.

ACKNOWLEDGMENTS

The National Service of Computational Chemistry Software (NSCCS) is thanked for providing generous CPU time. Research support was provided by the Department of Science

and Technology, India (SR/S1/IC-02/2009), and Council for Scientific & Industrial Research (01(2527)/11/EMR-II) to C.V.S. D.K. acknowledges Department of Science and Technology (New Delhi) for a Ramanujan Fellowship. A.S.F. thanks the Tertiary Education Trust Fund for a studentship.

REFERENCES

(1) (a) Sono, M.; Roach, M. P.; Coulter, E. D.; Dawson, J. H. *Chem. Rev.* **1996**, *96*, 2841−2888. (b) Groves, J. T. *Proc. Natl. Acad. Sci. U.S.A.* **2003**, *100*, 3569−3574. (c) Ortiz de Montellano, P. R., Ed. *Cytochrome P450: Structure, Mechanism and Biochemistry*, 3rd ed.; Kluwer Academic/Plenum Publishers: New York, 2004. (d) Denisov, I. G.; Makris, T. M.; Sligar, S. G.; Schlichting, I. *Chem. Rev.* **2005**, *105*, 2253−2277. (e) Kadish, K. M., Smith, K. M., Guilard, R., Eds. *Handbook of Porphyrin Science*; World Scientific: Hackensack, NJ, 2010. (f) Ortiz de Montellano, P. R. *Chem. Rev.* **2010**, *110*, 932−948. (g) O'Reilly, E.; Koehler, V.; Flitsch, S.; Turner, N. *Chem. Commun.* **2011**, *47*, 2490−2501. (h) Grogan, G. *Curr. Opin. Chem. Biol.* **2011**, *15*, 241−248.

(2) (a) Solomon, E. I.; Brunold, T. C.; Davis, M. I.; Kemsley, J. N.; Lee, S.-K.; Lehnert, N.; Neese, F.; Skulan, A. J.; Yang, Y.-S.; Zhou, J. *Chem. Rev.* **2000**, *100*, 235−349. (b) Bugg, T. D. H. *Curr. Opin. Chem. Biol.* **2001**, *5*, 550−555. (c) Costas, M.; Mehn, M. P.; Jensen, M. P.; Que, L., Jr. *Chem. Rev.* **2004**, *104*, 939−986. (d) Bruijnincx, P. C. A.; van Koten, G.; Klein Gebbink, R. J. M. *Chem. Soc. Rev.* **2008**, *37*, 2716−2744. (e) Bugg, T. D. H.; Ramaswamy, S. *Curr. Opin. Chem. Biol.* **2008**, *12*, 134−140. (f) Abu-Omar, M. M.; Loaiza, A.; Hontzeas, N. *Chem. Rev.* **2005**, *105*, 2227−2252. (g) Kryatov, S. V.; Rybak-Akimova, E. V.; Schindler, S. *Chem. Rev.* **2005**, *105*, 2175−2226. (h) Kovaleva, E. G.; Lipscomb, J. D. *Nat. Chem. Biol.* **2008**, *4*, 186−193. (i) He, P.; Moran, G. R. *Curr. Opin. Chem. Biol.* **2009**, *13*, 443−450.

(3) (a) Guengerich, F. P. *Chem. Res. Toxicol.* **2001**, *14*, 611−650. (b) Munro, A. W.; Girvan, H. M.; McLean, K. J. *Nat. Prod. Rep.* **2007**, *24*, 585−609.

(4) (a) Rittle, J.; Green, M. T. *Science* **2010**, *330*, 933−937. (b) de Visser, S. P.; Kumar, D., Eds., *Iron-Containing Enzymes: Versatile Catalysts of Hydroxylation Reactions in Nature*. RSC Publishing: Cambridge, U.K., 2011.

(5) (a) Groves, J. T. *J. Inorg. Biochem.* **2006**, *100*, 434−447. (b) Meunier, B.; de Visser, S. P.; Shaik, S. *Chem. Rev.* **2004**, *104*, 3947−3980.

(6) (a) White, R. E.; McCarthy, M. B. *J. Am. Chem. Soc.* **1984**, *106*, 4922−4926. (b) Svastits, E. W.; Dawson, J. H.; Breslow, R.; Gellman, S. H. *J. Am. Chem. Soc.* **1985**, *107*, 6427−6428. (c) Mahy, J.-P.; Bedi, G.; Battioni, P.; Mansuy, D. *J. Chem. Soc., Perkin Trans. II* **1988**, 1517−1524.

(7) (a) McIntosh, J. A.; Coelho, P. S.; Farwell, C. C.; Wang, Z. J.; Lewis, J. C.; Brown, T. R.; Arnold, F. H. *Angew. Chem., Int. Ed.* **2013**, *52*, 9309−9312. (b) Singh, R.; Bordeaux, M.; Fasan, R. *ACS Catal.* **2014**, *4*, 546−552.

(8) (a) Eikey, R. A.; Abu-Omar, M. M. *Coord. Chem. Rev.* **2003**, *243*, 83−124. (b) Berry, J. F. *Comments Inorg. Chem.* **2009**, *30*, 28−66. (c) Saouma, C. T.; Peters, J. C. *Coord. Chem. Rev.* **2011**, *255*, 920−937.

(9) (a) Bukowski, M. R.; Koehntop, K. D.; Stubna, A.; Bominaar, E. L.; Halfen, J. A.; Münck, E.; Nam, W.; Que, L., Jr. *Science* **2005**, *310*, 1000−1002. (b) Rohde, J.-U.; In, J.-H.; Lim, M. H.; Brennessel, W. W.; Bukowski, M. R.; Stubna, A.; Münck, E.; Nam, W.; Que, L., Jr. *Science* **2003**, *299*, 1037−1039. (c) Martinho, M.; Banse, F.; Bartoli, J.-F.; Mattioli, T. A.; Battioni, P.; Horner, O.; Bourcier, S.; Girerd, J.-J. *Inorg. Chem.* **2005**, *44*, 9592−9596. (d) Sastri, C. V.; Seo, M. S.; Park, M. J.; Kim, K. M.; Nam, W. *Chem. Commun.* **2005**, 1405−1407.

(10) (a) Che, C.-M.; Lo, V. K.-Y.; Zhou, C.-Y.; Huang, J.-S. *Chem. Soc. Rev.* **2011**, *40*, 1950−1975. (b) Lu, H.; Zhang, X. P. *Chem. Soc. Rev.* **2011**, *40*, 1899−1909. (c) Long, Z.; Liang, D. *Chin. Sci. Bull.* **2012**, *57*, 2352−2360. (d) Zdilla, M. J.; Dexheimer, J. L.; Abu-Omar, M. M. *J. Am. Chem. Soc.* **2007**, *129*, 11505−11511.

(11) See, for example, Zardi, P.; Caselli, A.; Macchi, P.; Ferretti, F.; Gallo, E. *Organometallics* **2014**, *33*, 2210−2218.

(12) (a) Scepaniak, J. J.; Bontchev, R. P.; Johnson, D. L.; Smith, J. M. *Angew. Chem., Int. Ed.* **2011**, *50*, 6630−6633. (b) Hohenberger, J.; Ray, K.; Meyer, K. *Nat. Commun.* **2012**, *3*, 1−13. (c) Torres-Alacan, J.; Das, U.; Filippou, A. C.; Vöhringer, P. *Angew. Chem., Int. Ed.* **2013**, *52*, 12833−12837. (d) Liu, Y.; Guan, X.; Wong, E. L.-M.; Liu, P.; Huang, J.-S.; Che, C.-M. *J. Am. Chem. Soc.* **2013**, *135*, 7194−7204. (e) Man, W.-L.; Xie, J.; Pan, Y.; Lam, W. W. Y.; Kwong, H.-K.; Ip, K.-W.; Yiu, S.-M.; Lau, K.-C.; Lau, T.-C. *J. Am. Chem. Soc.* **2013**, *135*, 5533−5536. (f) Man, W.-L.; Lam, W. W. Y.; Kwong, H.-K.; Yiu, S.-M.; Lau, T.-C. *Angew. Chem., Int. Ed.* **2012**, *51*, 9101−9104.

(13) Gouré, E.; Avenier, F.; Dubourdeaux, P.; Sénèque, O.; Albrieux, F.; Lebrun, C.; Clémancey, M.; Maldivi, P.; Latour, J.-M. *Angew. Chem., Int. Ed.* **2014**, *53*, 1580−1584.

(14) Klinker, E. J.; Jackson, T. A.; Jensen, M. P.; Stubna, A.; Juhász, G.; Bominaar, E. L.; Münck, E.; Que, L., Jr. *Angew. Chem., Int. Ed.* **2006**, *45*, 7394−7397.

(15) Vardhaman, A. K.; Barman, P.; Kumar, S.; Sastri, C. V.; Kumar, D.; de Visser, S. P. *Angew. Chem., Int. Ed.* **2013**, *52*, 12288−12292.

(16) Perrin, D. D., Ed., *Purification of Laboratory Chemicals*; Pergamon Press: Oxford, U.K., 1997.

(17) (a) Sharefkin, J. G., Ed. *Organic Syntheses*; Wiley: New York, 1973; Vol. *5*, p 658. (b) Taylor, S.; Gullick, J.; McMorn, P.; Bethell, D.; Bulman Page, P. C.; Hancock, F. E.; King, F.; Hutchings, G. J. *J. Chem. Soc., Perkin Trans. II* **2001**, 1714−1723.

(18) (a) Lubben, M.; Meetsma, A.; Wilkinson, E. C.; Feringa, B.; Que, L., Jr. *Angew. Chem., Int. Ed.* **1995**, *34*, 1512−1515. (b) Vardhaman, A. K.; Barman, P.; Kumar, S.; Sastri, C. V.; Kumar, D.; de Visser, S. P. *Chem. Commun.* **2013**, *49*, 10926−10928.

(19) (a) Kaizer, J.; Klinker, E. J.; Oh, N. Y.; Rohde, J.-U.; Song, W. J.; Stubna, A.; Kim, J.; Münck, E.; Nam, W.; Que, L., Jr. *J. Am. Chem. Soc.* **2004**, *126*, 472−473. (b) Vardhaman, A. K.; Sastri, C. V.; Kumar, D.; de Visser, S. P. *Chem. Commun.* **2011**, *47*, 11044−11046.

(20) (a) *Jaguar*, version 7.9, Schrodinger, LLC: New York, NY, 2011. (b) Frisch, M. J. et al. *Gaussian 09*, revision C.01; Gaussian, Inc.: Wallingford, CT, 2010.

(21) Cossi, M.; Barone, V.; Cammi, R.; Tomasi, J. *Chem. Phys. Lett.* **1996**, *255*, 327−335.

(22) See, for example, (a) Latifi, R.; Sainna, M. A.; Rybak-Akimova, E. V.; de Visser, S. P. *Chem.—Eur. J.* **2013**, *19*, 4058−4068. (b) Quesne, M. G.; Latifi, R.; Gonzalez-Ovalle, L. E.; Kumar, D.; de Visser, S. P. *Chem.—Eur. J.* **2014**, *20*, 435−446. (c) de Visser, S. P.; Quesne, M. G.; Martin, B.; Comba, P.; Ryde, U. *Chem. Commun.* **2014**, *50*, 262−282.

(23) (a) Becke, A. D. *J. Chem. Phys.* **1993**, *98*, 5648−5652. (b) Lee, C.; Yang, W.; Parr, R. G. *Phys. Rev. B* **1988**, *37*, 785−789.

(24) Hay, P. J.; Wadt, W. R. *J. Chem. Phys.* **1985**, *82*, 270−283.

(25) Grimme, S. *J. Chem. Phys.* **2006**, *124*, No. 034108.

(26) (a) Becke, A. D. *Phys. Rev. A* **1988**, *38*, 3098−3100. (b) Perdew, J. P. *Phys. Rev. B* **1986**, *33*, 8822−8824.

(27) Adamo, C.; Barone, V. *J. Chem. Phys.* **1999**, *110*, 6158−6169.

(28) Zhao, Y.; Truhlar, D. G. *Theor. Chem. Acc.* **2008**, *120*, 215−241.

(29) (a) de Visser, S. P. *Chem.—Eur. J.* **2006**, *12*, 8168−8177. (b) Heyes, D. J.; Sakuma, M.; de Visser, S. P.; Scrutton, N. S. *J. Biol. Chem.* **2009**, *284*, 3762−3767.

(30) Ji, L.; Zhang, J.; Liu, W.; de Visser, S. P. *Chem.—Asian J.* **2014**, *9*, 1175−1182.

(31) Nam, W.; Lee, Y.-M.; Fukuzumi, S. *Acc. Chem. Res.* **2014**, *47*, 1146−1154.

(32) Oh, N. Y.; Suh, Y.; Park, M. J.; Seo, M. S.; Kim, J.; Nam, W. *Angew. Chem., Int. Ed.* **2005**, *44*, 4235−4239.

(33) Cheng, W.-C.; Yu, W.-Y.; Li, C.-K.; Che, C.-M. *J. Org. Chem.* **1995**, *60*, 6840−6846.

(34) See, for example, (a) Meyer, K.; Roček, J. *J. Am. Chem. Soc.* **1972**, *94*, 1209−1214. (b) Pestovsky, O.; Bakac, A. *J. Am. Chem. Soc.* **2004**, *126*, 13757−13764. (c) Hanson, S. K.; Baker, R. T.; Gordon, J. C.; Scott, B. L.; Silks, L. A.; Thorn, D. L. *J. Am. Chem. Soc.* **2010**, *132*, 17804−17816.

(35) (a) Kumar, D.; Hirao, H.; Que, L., Jr.; Shaik, S. *J. Am. Chem. Soc.* **2005**, *127*, 8026−8027. (b) Hirao, H.; Kumar, D.; Que, L., Jr; Shaik, S. *J. Am. Chem. Soc.* **2006**, *128*, 8590−8606.
(36) (a) de Visser, S. P. *J. Am. Chem. Soc.* **2006**, *128*, 15809−15818. (b) de Visser, S. P. *Angew. Chem., Int. Ed.* **2006**, *45*, 1790−1793. (c) Ye, S.; Neese, F. *Proc. Natl. Acad. Sci. U.S.A.* **2011**, *108*, 1228−1233.
(37) (a) Karamzadeh, B.; Singh, D.; Nam, W.; Kumar, D.; de Visser, S. P. *Phys. Chem. Chem. Phys.* **2014**, *16*, 22611−22622. (b) de Visser, S. P.; Tan, L. S. *J. Am. Chem. Soc.* **2008**, *130*, 12961−12974.
(38) (a) Zhao, Y.; Truhlar, D. G. *Acc. Chem. Res.* **2008**, *41*, 157−167. (b) Schwabe, T.; Grimme, S. *Acc. Chem. Res.* **2008**, *41*, 569−579. (c) Weymuth, T.; Couzijn, E. P. A.; Chen, P.; Reiher, M. *J. Chem. Theory Comput.* **2014**, *10*, 3092−3103.
(39) (a) de Visser, S. P. *J. Am. Chem. Soc.* **2010**, *132*, 1087−1097. (b) Kumar, D.; Karamzadeh, B.; Sastry, G. N.; de Visser, S. P. *J. Am. Chem. Soc.* **2010**, *132*, 7656−7667. (c) Kumar, D.; Latifi, R.; Kumar, S.; Rybak-Akimova, E. V.; Sainna, M. A.; de Visser, S. P. *Inorg. Chem.* **2013**, *52*, 7968−7979.
(40) Kumar, D.; de Visser, S. P.; Sharma, P. K.; Cohen, S.; Shaik, S. *J. Am. Chem. Soc.* **2004**, *126*, 1907−1920.
(41) de Visser, S. P.; Ogliaro, F.; Shaik, S. *Angew. Chem., Int. Ed.* **2001**, *40*, 2871−2874.
(42) Kumar, D.; Tahsini, L.; de Visser, S. P.; Kang, H. Y.; Kim, S. J.; Nam, W. *J. Phys. Chem. A* **2009**, *113*, 11713−11722.
(43) (a) Conradie, J.; Ghosh, A. *Inorg. Chem.* **2010**, *49*, 243−248. (b) Jaccob, M.; Rajaraman, G. *Dalton Trans.* **2012**, *41*, 10430−10439.
(44) Leeladee, P.; Baglia, R. A.; Prokop, K. A.; Latifi, R.; de Visser, S. P.; Goldberg, D. P. *J. Am. Chem. Soc.* **2012**, *134*, 10397−10400.
(45) (a) Shaik, S.; Kumar, D.; de Visser, S. P. *J. Am. Chem. Soc.* **2008**, *130*, 10128−10140. (b) Shaik, S. *Phys. Chem. Chem. Phys.* **2010**, *12*, 8706−8720. (c) Shaik, S.; Lai, W.; Chen, H.; Wang, Y. *Acc. Chem. Res.* **2010**, *43*, 1154−1165.
(46) Shaik, S. S. *J. Am. Chem. Soc.* **1981**, *103*, 3692−3701.
(47) Fernández, I.; Frenking, G. *Chem. Commun.* **2006**, 5030−5032.
(48) See, for example, (a) Bordwell, F. G.; Cheng, J.-P.; Ji, G.-Z.; Satish, A. V.; Zhang, X. *J. Am. Chem. Soc.* **1991**, *113*, 9790−9795. (b) Mayer, J. M. *Acc. Chem. Res.* **1998**, *31*, 441−450. (c) Goldberg, D. P. *Acc. Chem. Res.* **2007**, *40*, 626−634. (d) Kang, Y.; Chen, H.; Jeong, Y. J.; Lai, W.; Bae, E. H.; Shaik, S.; Nam, W. *Chem.—Eur. J.* **2009**, *15*, 10039−10046.
(49) Green, M. T.; Dawson, J. H.; Gray, H. B. *Science* **2004**, *304*, 1653−1656.
(50) Lias, S. G. Ionization energy evaluation. In *NIST Chemistry Webbook*; Linstrom, P. J., Mallard, W. G., Eds.; NIST Standard Reference Database Number 69; National Institute of Standards andTechnology: Gaithersburg, MD, 2009; 20899 (http://webbook.nist.gov).
(51) (a) Sharma, P. K.; de Visser, S. P.; Shaik, S. *J. Am. Chem. Soc.* **2003**, *125*, 8698−8699. (b) Prokop, K. A.; Neu, H. M.; de Visser, S. P.; Goldberg, D. P. *J. Am. Chem. Soc.* **2011**, *133*, 15874−15877. (c) Kumar, D.; Sastry, G. N.; de Visser, S. P. *Chem.—Eur. J.* **2011**, *17*, 6196−6205.
(52) Shaik, S.; Wang, Y.; Chen, H.; Song, J.; Meir, R. *Faraday Discuss.* **2010**, *145*, 49−70.